

Parkinson's Disease-Associated LRRK2 Interferes with Astrocyte-Mediated Alpha-Synuclein Clearance

Linn Streubel-Gallasch

Uppsala University

Veronica Giusti

University of Padova: Università degli Studi di Padova

Michele Sandre

University of Padova: Università degli Studi di Padova

Isabella Tessari

University of Padova: Università degli Studi di Padova

Nicoletta Plotegher

University of Padova: Università degli Studi di Padova

Elena Giusto

San Camillo Hospital: Ospedale San Camillo

Anna Masato

University of Padova: Università degli Studi di Padova

Ludovica Iovino

University of Padova: Università degli Studi di Padova

Ilaria Battisti

University of Padova: Università degli Studi di Padova

Giorgio Arrigoni

University of Padova: Università degli Studi di Padova

Elisa Greggio

University of Padova: Università degli Studi di Padova

Marie-Eve Tremblay

University of Victoria

Luigi Bubacco

University

Anna Erlandsson

Uppsala University: Uppsala Universitet

Laura Civiero (✉ laura.civiero@unipd.it)

University of Padova Department of Biology: Università degli Studi di Padova Dipartimento di Biologia

Keywords: Parkinson's disease, α -synuclein, LRRK2, astrocytes, glia, neurodegeneration

Posted Date: October 26th, 2020

DOI: <https://doi.org/10.21203/rs.3.rs-95404/v1>

License:  This work is licensed under a Creative Commons Attribution 4.0 International License.

[Read Full License](#)

Version of Record: A version of this preprint was published at Molecular Neurobiology on February 24th, 2021. See the published version at <https://doi.org/10.1007/s12035-021-02327-8>.

Parkinson's disease-associated LRRK2 interferes with astrocyte-mediated alpha-synuclein clearance

Linn Streubel-Gallasch^{*1}, Veronica Giusti^{*2}, Michele Sandre^{3, 4}, Isabella Tessari², Nicoletta Plotegher², Elena Giusto⁵, Anna Masato², Ludovica Iovino², Ilaria Battisti⁶, Giorgio Arrigoni^{6,7}, Elisa Greggio², Marie-Eve Tremblay⁸, Luigi Bubacco², Anna Erlandsson^{^#1} and Laura Civiero^{^#2,5}

¹ Department of Public Health and Caring Sciences, Uppsala University, Sweden

² Department of Biology, University of Padova, Italy

³ Parkinson and Movement Disorders Unit, Department of Neuroscience, University of Padova, Italy

⁴ PNC, Padua Neuroscience Center, University of Padova, Italy

⁵ IRCCS San Camillo Hospital, Venice, Italy

⁶ Department of Biomedical Sciences, University of Padova, Italy

⁷ CRIBI Biotechnology Center, University of Padova

⁸ Division of Medical Sciences, University of Victoria, Victoria, Canada

^{*} The authors contributed equally to the work

[^] Shared last authorship

[#] Correspondence: laura.civiero@unipd.it and anna.erlandsson@pubcare.uu.se;

Abstract

Background

Parkinson's disease (PD) is a neurodegenerative, progressive disease without cure. To prevent PD onset or at least limit neurodegeneration, a better understanding of the underlying cellular and molecular disease mechanisms is crucial. Mutations in the leucine rich repeat kinase 2 (*LRRK2*) gene represent one of the most common causes of familial PD. In addition, *LRRK2* variants are risk factors for sporadic PD, making *LRRK2* an attractive therapeutic target. Mutations in *LRRK2* has been linked to impaired alpha-synuclein (α -syn) degradation in neurons. However, in which way pathogenic *LRRK2* affects α -syn clearance by astrocytes, the major glial cell type of the brain, remains unclear. The impact of astrocytes on PD progression has recently received much attention and recent data indicate that astrocytes play a key role in α -syn mediated pathology.

Methods

In the present study, we aimed to compare the capacity of wild-type astrocytes and astrocytes carrying the PD-linked G2019S mutation in *Lrrk2* to ingest and degrade fibrillary α -syn. For this purpose, we used two different astrocyte culture systems that were exposed to sonicated α -syn for 24 hours and analyzed directly after the α -syn pulse or 6 days later. To elucidate the impact of *LRRK2* on α -syn clearance, we performed various analyses, including complementary imaging, transmission electron microscopy and proteomic approaches.

Results

Our results show that astrocytes carrying the G2019S mutation in *Lrrk2* exhibit a decreased capacity to internalize and degrade fibrillar α -syn *via* the endo-lysosomal pathway. In addition, we demonstrate that the reduction of α -syn internalization in the *Lrrk2* G2019S astrocytes is linked to Annexin A2 (AnxA2) loss-of-function.

Conclusion

Together, our findings reveal that astrocytic LRRK2 contributes to the clearance of extracellular α -syn aggregates through an AnxA2-dependent mechanism.

Keywords: Parkinson's disease, α -synuclein, LRRK2, astrocytes, glia, neurodegeneration

Background

Parkinson's disease (PD) is the second most common neurodegenerative disease. Yet, there is no cure available and much is unknown regarding the underlying disease mechanisms. PD patients primarily suffer from severe motor deficiencies, but also develop non-motor symptoms, including loss of smell, sleep disturbance, depression and dementia [1]. The main pathological hallmarks of PD are i) degeneration of dopaminergic neurons in *substantia nigra pars compacta* and ii) intracellular inclusions of insoluble alpha-synuclein (α -syn) fibrils [2]. In addition to neuronal inclusions, α -syn deposits appear frequently in astrocytes, at all stages of PD [3-7]. Recent data from our research group suggest that the internalization and accumulation of fibrillar α -syn in astrocytes may play an important role in PD progression and associated chronic neuroinflammation [8, 9]. However, the precise molecular pathways crucial for α -syn clearance by astrocytes currently remain unclear. The aim of the present study was to investigate the role of leucine rich repeat kinase 2 (LRRK2) in the uptake and degradation of fibrillary α -syn by primary cultured astrocytes.

LRRK2 is a multi-module kinase protein, expressed in various organs and cell types including astrocytes [10-12]. Mutations in LRRK2 are the most frequent cause of familial PD, with seven pathogenic mutations identified (G2019S, I2020T, R1441C/G/H, Y1699C, N1437H) [13]. Because all mutations increase kinase activity in cells [14], LRRK2 is one of the most pursued therapeutic targets in PD. The common G2019S (GS) mutation accounts for ~ 1% of sporadic PD and up to 40% of familial PD in certain populations [15]. LRRK2 exerts pleiotropic effects at the cellular level by regulating multiple steps of vesicle trafficking and cytoskeletal dynamics [14, 16-18]. Accumulating evidence suggests that LRRK2 controls endogenous α -syn clearance via the endo-lysosomal pathway both *in vitro* and *in vivo* [19-21]. Moreover, LRRK2 regulates the ingestion of extracellular material by different phagocytic cells. Macrophages and microglia

93 derived from LRRK2 G2019S patients and mice display increased phagocytic capacity, while
94 loss of LRRK2 was shown to induce phagocytic deficits in myeloid cells [22]. In line with these
95 findings, inhibition of LRRK2 kinase activity blocks phagocytosis in microglial cells [23] and
96 normalizes lysosome defects in GBA1-mutant astrocytes [24]. However, LRRK2 has also been
97 shown to impair phagosome maturation in macrophages [25], and to be recruited at later stages
98 of the internalization in macrophages and microglia [26], indicating that a clear understanding
99 of LRRK2's role in phagocytosis is missing. Of note, a recent report indicates that LRRK2
100 negatively regulates clearance of extracellular particles *via* macropinocytosis [27].

101
102 Despite intensive research progress, the exact mechanisms by which LRRK2 mutations lead to
103 neurodegeneration remain largely unclear, especially, when it comes to astrocytes. Being the
104 most abundant glial cell, astrocytes play an important role in maintaining brain homeostasis
105 [28]. Their functions include metabolic support to neurons, modification of synapse signalling,
106 recycling of neurotransmitters and contribution to the blood-brain barrier required to prevent
107 homeostatic disturbance and inflammation from the periphery. In the PD brain, astrocytes are
108 converted to a reactive, inflammatory state in which they phagocytose aggregated proteins and
109 cell debris, as well as secrete various cytokines and chemokines. Our previous data show that
110 heavy materials, such as dead cell debris and aggregated, pathogenic proteins are internalized
111 and stored in the astrocytes, rather than digested [9, 29-32].

112
113 Compelling evidence demonstrate that pathological α -syn can transfer from cell-to-cell in the
114 PD brain and thereby contribute to disease progression. In cell culture experiments, aggregated
115 α -syn can transfer from neurons to astrocytes and from one astrocyte to another [9, 33]. Hence,
116 regulation of α -syn uptake by astrocytes may indirectly have an impact on PD progression. In

117 the present study we show that LRRK2 affects α -syn uptake, rather than its degradation, in
118 cultured astrocytes in several ways.

119

Methods

Animals

C57Bl/6J *Lrrk2* wild-type (*Lrrk2*^{+/+}) and knock-out (*Lrrk2*^{-/-}) mice, were respectively provided by Dr. Heather Melrose and Jackson Laboratory [B6.129X1 (FVB)-*Lrrk2*^{tm1.1Cai/J}] [34, 35]. *Lrrk2* G2019S knock-in mice, backcrossed on a C57Bl/6J background, were used. *Lrrk2* G2019S knock-in mice (*Lrrk2*^{GS/GS}) were obtained from Prof. Michele Morari and Novartis Institutes for BioMedical Research, Novartis Pharma AG (Basel, Switzerland) [36]. Housing and handling of mice were done in compliance with national guidelines. All animal procedures were approved by the Ethical Committee of the University of Padova and the Italian Ministry of Health (license 46/2012 and 105/2019).

Cortical stem-cell derived astrocytes

Mouse embryonic cortices (gestation days 12-14) were dissected in Hank's Buffered Salt Solution supplemented with 100 U/ml penicillin, 100 µg/ml streptomycin and 8 mM Hepes buffer (HBSS; all Gibco) and dissociated by brief trituration. Blood cells were allowed to sediment for 10 min. The supernatant was transferred and the cells collected by centrifugation (100 x g, 5 min) followed by careful re-suspension in serum-free proliferation medium containing Dulbecco's Modified Eagle Medium (DMEM)/F12 with GlutaMAX, 1x B27 supplement, 100 U/ml penicillin, 100 µg/ml streptomycin, 8 mM Hepes buffer (all Gibco) and fortified with 10 ng/ml, basic Fibroblast Growth Factor (bFGF, Gibco) and 20 ng/ml Epidermal Growth Factor (EGF, Corning). The embryonic cortical stem cells were allowed to expand as neurospheres in non-treated tissue cultures flasks (at 37°C, 5% CO₂) with a passage every two to three days comprising a thorough dissociation in HBSS and re-suspension in proliferation medium (compositions as described above). For experiments, neurospheres were dissociated in HBSS, taking care to reach a single cell suspension, and seeded as a monolayer at a density of

2x10⁴ cells/cm² on cover glasses coated with poly-L-ornithine (Sigma-Aldrich) and laminin (Gibco). For the first 24 h, cells were cultured (at 37°C, 5% CO₂) in proliferation medium, thereafter in mitogen-free differentiation medium containing DMEM/F12 with GlutaMAX, 1x B27 supplement, 100 U/ml penicillin, 100 µg/ml streptomycin, 8 mM Hepes buffer (all Gibco), which was fully replaced every two to three days during the seven-day differentiation period. Being based on embryonic, cortical stem cells, this well characterized cell culture system solely contains cells of the neural lineage [29, 37-39]. Differentiation led to a mixed population of 75 ± 8% astrocytes, 25 ± 8% neurons and 6 ± 3% oligodendrocytes, without any microglia or macrophages, as expected from the literature [31, 32, 40]. Independent experiments were carried out using cells obtained from embryos of different pregnant mice.

Primary striatal astrocytes

Mouse primary striatal astrocytes were obtained from postnatal animals between days 1 and 3. Brains were dissected from skull and placed in a dish, containing cold Dulbecco's Phosphate Buffered Saline (DPBS, Biowest). Olfactory bulbs and cortices were removed under an optic microscope and striatum was transferred to a separate dish containing cold DPBS. After the dissection, Basal Medium Eagle (BME, Biowest), supplemented with 10% Fetal Bovine Serum (FBS, Corning), 100 U/ml penicillin and 100 µg/ml streptomycin, was added to the tissues. Striata were then sifted through a 70 µm cell strainer (Sarstedt), using a syringe plunger. The cell suspension was centrifuged (300 x g, 15 min) and the pellet was washed two times with 25 ml of supplemented medium. Cells were seeded at a density of 5x10⁶ cells/10 ml medium in cell culture flasks. The culture medium was changed after seven days and again after additional 3-4 days. When cell confluency reached about 80%, microglia were detached by shaking the flask (800 rpm) for 2 h at room temperature (RT). After shaking, the medium containing microglia was replaced with fresh medium. Cells were maintained in BME supplemented with

168 10% FBS, 100 U/ml penicillin, 100 µg/ml streptomycin at 37°C in controlled 5% CO₂
169 atmosphere. Independent experiments were carried out using cells obtained from different pups.

170 *Immortalized H4 cells*

171 Human H4 neuroglioma cells were kindly provided by Prof. Patrick A. Lewis (The Royal
172 Veterinary College, London, UK). H4 cells were cultured in DMEM (Biowest) supplemented
173 with 10% FBS (Corning), 100 U/ml penicillin, and 100 µg/ml streptomycin at 37°C and 5%
174 CO₂. Cells were plated on 100 mm Ø dishes (Corning) at a density of 5x10⁶ cells/10 ml medium
175 for purification procedure or on 12 mm Ø glass coverslips (Thermo-Scientific) at a density of
176 0.1x10⁶ cells for immunocytochemistry experiments.

177 *Cell transfection*

178 Once reached 80% of confluency in 100 mm Ø dishes, H4 cells were transiently transfected
179 with 10 µg of pCHMWS-3xflag-LRRK2 plasmids encoding for human LRRK2 [41] and 5 µg
180 of pEGFP-N3-AnxA2-GFP encoding for human Annexin A2 (Addgene, #107196), using linear
181 polyethylenimine (PEI, Polysciences) and following 1:2 DNA:PEI ratio. On 12 mm Ø glass
182 coverslips, H4 cells were transiently transfected with 2 µg of pEGFP-N3-AnxA2-GFP at 60%
183 of confluency. DNA and PEI were diluted in OPTIMEM (Gibco) and incubated for 20 min at
184 RT to allow the formation of DNA/PEI complexes. The mix was added to cells and the
185 experimental procedure was carried out after 48 h. Primary striatal astrocytes were seeded in
186 24-well plates at the seeding density of 0.025 x 10⁶/well. Cells were transfected with mouse
187 AnxA2 siRNA SMARTPool at a final concentration of 50 nM (Dharmacon) using
188 Lipofectamine 2000 (Thermo Scientific) following 1:3 siRNA:Lipofectamine ratio. After 72 h,
189 the experimental procedure was carried out.

190 *Alpha-synuclein*

191 To generate α -syn pre-formed fibrils (PFFs), *in-house* purified as in [42] or commercial
192 (Anaspec #AS-55555) human α -syn monomers reconstituted at a concentration of 5 mg/ml in
193 sterile DPBS (Gibco) and sterile-filtered (Costar Spin-X centrifuge tube filters (Merck),
194 0.45 μ m), were incubated on a shaker (IKA MS3 Basic or ThermoMixer F1.5 Eppendorf,
195 1000 rpm) at 37°C for seven days. α -syn PFFs were diluted to a stock concentration in sterile
196 PBS and stored at -70°C. Both unlabeled and Cy3- or SNARF-1 C2-Maleimide-labeled α -syn
197 PFFs were used in this study.

198 α -syn was labeled using a Cy3 labeling kit (GE Healthcare #PA33000) in accordance with
199 manufacturer's instructions. Briefly, 1 mg of α -syn PFFs were mixed with coupling buffer and
200 added to the Cy3 dye. After a 1 h labelling reaction at RT, unbound Cy3 dye was removed by
201 the following wash procedure, which was repeated three times: centrifugation (20000 \times g, 30
202 min), removal of supernatant and resuspension of the pellet in sterile PBS. Cy3-labelled α -syn
203 PFFs were stored at -70°C.

204 α -syn monomer presenting two additional residues at C-terminal position (α -syn Gly-Cys) was
205 prepared as described previously [42, 43] and labeled with SNARF-1 C2-Maleimide dye
206 (Setareh Biotech). SNARF molecule absorbs at 488 nm and changes the emission spectrum at
207 550 and 630 nm according to the environmental pH. Specifically, the ratio 550/630 nm
208 enhances upon a decrease in pH. By following the procedure described in [44], reduced α -syn
209 Gly-Cys monomer was diluted 1:1 in water and EDTA (1mM) pH 8 with the addition of 70%
210 ammonium sulfate salt (w/v). Labelling reaction was achieved by adding 5 molar equivalents
211 of SNARF-1 C2-Maleimide dye and incubating at RT overnight. SNARF-1 labelled α -syn was
212 precipitated by centrifugation (20000 \times g, 10 min, 4°C) and the exceeding dye was removed
213 through PD-10 column (GE Healthcare). To generate SNARF-1-labelled PFFs, monomers of
214 α -syn and SNARF-labelled α -syn were incubated in a 10:1 ratio. Fluorescence spectra of both
215 free SNARF-1 molecule and SNARF-1 labelled PFFs were analyzed at different pH using a

216 Cary Eclipse Fluorescence Spectrophotometer (Varian), exciting at 488 nm and collecting
217 spectra within 520-660 nm.

218 Just before use, labeled and unlabeled α -syn PFFs were diluted to a concentration of 1 mg/ml
219 in sterile PBS and sonicated at a power input between 20-30 W for 30 s (pulsing on/off) at 4°C
220 (Sonics Vibra Cell sonicator or Covaris S2 Ultrasonicator). Characterization of α -syn PFFs was
221 performed by transmission electron microscopy (TEM) using negative staining. α -syn PFFs
222 were diluted 1:10 in distilled H₂O and placed on a formvar and carbon coated 200-mesh copper
223 grid (Ted Pella). The sample was directly stained with 2% uranyl acetate. Dried grids were
224 examined by TEM (FEI Tecnai G2) operated at 80 kV with an ORIUS SC200 CCD camera
225 and Gatan Digital Micrograph software (both Gatan Inc.).

226 *Alpha-synuclein exposure*

227 Cells were exposed to sonicated Cy3-labeled, SNARF-1-labeled or unlabeled α -syn PFFs at a
228 concentration of 0.5 μ M for 24 h. Cells were then rinsed twice with culture medium to remove
229 any excess α -syn PFFs. Subsequently, cells were either processed for immunocytochemistry,
230 western blot or live-imaging assay (24 h time-point). For cortical stem-cell derived cultures,
231 medium samples were collected at the moment of α -syn PFF addition to the cells (0 h time-
232 point) as well as after the 24 h exposure to α -syn PFFs (before the wash procedure). The cells
233 were then either processed for analysis or cultured in differentiation medium (DMEM/F12 with
234 GlutaMAX, 1x B27 supplement, 100 U/ml penicillin, 100 μ g/ml streptomycin, 8 mM Hepes
235 buffer (all Gibco)) for six additional days (24 h + 6 d time-point).

236 *Immunocytochemistry*

237 Cells were fixed in 4% paraformaldehyde (PFA)/PBS for 20 min at RT, followed by two washes
238 in PBS. Then, cells were permeabilized and blocked in 0.1% Triton X-100/PBS with 5%
239 Normal Goat Serum (NGS) for 30 min at RT or with 5% v/v FBS in PBS for 60 min at RT.

Primary antibody incubation was performed using: chicken polyclonal glial fibrillary acidic protein (GFAP) (Abcam #ab4674, 1:400), rat monoclonal lysosome-associated protein (Lamp-1) (clone 1D4B) (Abcam #ab25245, 1:100), rabbit polyclonal lysosome-associated membrane protein (Lamp2A) (Abcam #ab18528, 1:200), purified mouse anti- α -Synuclein (BD Laboratories #610787, 1:400), rabbit polyclonal Annexin II (Genetex International #GTX101902, 1:200). Secondary antibody incubation was carried out for 30 min at 37°C or for 1 h at RT using anti-chicken Alexa Fluor 647 (Invitrogen #A21449), anti-rabbit Alexa Fluor 488 (Invitrogen #A11034), anti-mouse Alexa Fluor 568 (Invitrogen #A11004) fluorophores. Secondary antibodies were diluted 1:200 in 0.1% Triton X-100/PBS with 0.5% NGS or with 5%v/v FBS in PBS. Both primary and secondary antibody incubations were followed by three washes in PBS for 5 min. In some experiments, cells were stained using Phalloidin-iFluor 647 Reagent (Abcam #ab176759). Cover glasses were mounted on a microscope slide (Thermo Scientific) using EverBrite hardset mounting medium (Biotium) or Mowiol (Calbiochem) supplied with DAPI and, in some experiments, in combination with Vectashield HardSet antifade mounting medium with TRITC-Phalloidin (Vector Laboratories).

Transmission electron microscopy and image analysis

Primary striatal astrocytes were seeded onto 24 wells plates (10×10^4 cells) and fixed at 80% confluency. The medium was removed and fixative buffer (glutaraldehyde 2.5% in 0.1 M sodium cacodylate buffer) was added to the cells for 1 h at 4°C. Then, the samples were post-fixed using 1% osmium tetroxide plus potassium ferrocyanide 1% in 0.1 M sodium cacodylate buffer for 1 h at 4°. After three washes with water, samples were dehydrated in a graded ethanol series and embedded in epoxy resin (Epoxy Embedding Medium kit, Sigma-Aldrich). Ultrathin sections (60-70 nm) were obtained with an Ultratome V (LKB) ultramicrotome, counterstained

with uranyl acetate and lead citrate, and viewed with a Tecnai G2 (FEI) transmission electron microscope operating at 100 kV. Images were captured, using a Veleta (Olympus Soft Imaging System) magnification 9800x digital camera. Electron microscopy images were analyzed using ImageJ and blind to the experimental conditions. We identified lysosomal-like structures using the following ultrastructural features: 0.05 - 0.5 μm in diameter and granular, electron-dense appearance in electron micrographs [45]. Lysosomal-like structures were counted and their areas were determined using the oval selection tool of the Region of Interest (ROI) Manager tool (ImageJ). Lysosomal-like structure numbers were normalized to the field area. Number of independent cell cultures used: *Lrrk2*^{+/+} n = 4, *Lrrk2*^{-/-} n = 4 and *Lrrk2*^{GS/GS} n = 4. For each cell culture, fifty independent fields were analyzed for quantification.

Fluorescence microscopy and image analysis

For cortical stem-cell derived astrocytes studies, images were taken with a Zeiss Axio Observer Z1 fluorescence microscope equipped with a 40x/0.93 NA plan-apochromat objective and a 63x/1.40 oil DIC plan-apochromat objective. Images were acquired at a 16-bit intensity resolution over 2048 x 2048 pixels. Number of independent cell cultures used: *Lrrk2*^{+/+} n = 7, *Lrrk2*^{-/-} n = 6 and *Lrrk2*^{GS/GS} n = 5 at the 24 h time-point and *Lrrk2*^{+/+} n = 6, *Lrrk2*^{-/-} n = 6 and *Lrrk2*^{GS/GS} n = 5 at 24 h + 6 d. For each culture, ten independent fields per cover glass were evaluated and reported. Cy3 α -syn inclusions were analyzed using ImageJ. An ImageJ macro was developed that included the following steps: set scale, convert to 8-bit, subtract background, set threshold (the same threshold was used for both time-points), set measurements and analyze particles. In each image, Cy3 α -syn deposits were assessed by measuring the total area taken up by the Cy3 signal, by the number of particles counted as well as by the sum of the integrated densities (area x mean intensity of each Cy3 α -syn deposit). Analysis results were normalized to the number of living cells (identified by DAPI staining). Since various sized Cy3 α -syn inclusions were observed, the ImageJ macro was adjustable to quantify different types of

inclusions separately. Judging by the area measurements of the various particles, the cut-off limit for the group of small Cy3 α -syn particles was set at $\leq 25 \mu\text{m}^2$. Quantifications for larger ($>25 \mu\text{m}^2$) Cy3 α -syn particles were obtained by subtracting the area/ particle count/integrated density information of the small Cy3 α -syn particles from numbers acquired when quantifying all Cy3 α -syn particles.

For primary striatal astrocytes – live imaging studies, images were acquired at 8-bit intensity resolution over 1024x1024 pixel, through Leica SP5 confocal microscope, using a HC PL FLUOTAR 20x/0.50 dry objective. Number of independent cell cultures used: *Lrrk2*^{+/+} n = 4, *Lrrk2*^{-/-} n = 4 and *Lrrk2*^{GS/GS} n = 4. Pictures were acquired at the two relevant ranges of the emission spectrum (channel1: 530-550 nm and channel2: 610-630 nm). For each culture, six to eight independent fields were evaluated and reported. SNARF-1-positive α -syn inclusions were analyzed using ImageJ. SNARF-1-labeled α -syn PFFs were assessed using an ImageJ macro including the following steps: set scale, convert to 8-bit, subtract background, set threshold, set measurements and analyze particles. The ratio of the single-particle integrated density (area x mean intensity) between channel1 and channel2 and number of particles per ROI were measured. ROIs were first identified in channel1 and then transferred to channel2.

For primary striatal astrocytes – post-fixation imaging, images were acquired at 8-bit intensity resolution over 1024 x 1024 pixels, through Leica SP5 confocal microscope using a HC PL FLUOTAR 40x/0.70 dry objective. Lamp2A-positive puncta were counted using Analyzed particles plug-in in ImageJ. Fluorescent puncta were assessed by area and particles count. Number of independent cell cultures used for evaluation of Lamp2A-positive puncta in *Lrrk2*^{+/+} versus *Lrrk2*^{-/-} versus *Lrrk2*^{GS/GS} astrocytes: *Lrrk2*^{+/+} n = 3, *Lrrk2*^{-/-} n=3 and *Lrrk2*^{GS/GS} n = 3. For each culture, eight independent fields per experiment were evaluated and reported.

Proximity analysis for AnxA2 and unlabeled α -syn PFFs dots was performed using ComDet plug-in in ImageJ ([https://imagej.net/Spots_colocalization_\(ComDet\)](https://imagej.net/Spots_colocalization_(ComDet))), using the following parameters: max co-localization distance (0.9 pixel) and particles dimension (AnxA2: 3 pixels and α -syn: 4 pixels). The number of AnxA2 dots and the number of α -syn puncta was assessed by ‘puncta count’ output and the proximity between AnxA2 dots and engulfed α -syn as ‘co-localization’ output. All quantifications were normalized to the number of living cells identified by nuclei staining. Number of independent cell cultures used in AnxA2 downregulation experiments: *Lrrk2*^{+/+} n = 3. For each culture, four independent fields per experiment were evaluated and reported. Number of independent cell cultures used for evaluation of AnxA2 function in *Lrrk2*^{+/+} versus *Lrrk2*^{GS/GS} astrocytes: *Lrrk2*^{+/+} n = 3 and *Lrrk2*^{GS/GS} n = 3. For each culture, eight independent fields per experiment were evaluated and reported.

Protein purification

3xFlag-LRRK2 purification was performed as described in [41]. Briefly, transfected H4 cells were solubilized in an appropriate volume of radioimmunoprecipitation assay buffer, RIPA buffer (20 mM Tris-HCl pH 7.5, 150 mM NaCl, 1 mM EDTA, 2.5 mM sodium pyrophosphate - Na₄P₂O₇, 1 mM β -glycerophosphate - C₃H₇Na₂O₆P, 1 mM sodium orthovanadate - Na₃VO₄) containing 1% protease inhibitor cocktail (Sigma-Aldrich). Lysates were centrifugated for 30 min at 14000 \times g. Afterwards, lysates containing 3xFlag-tagged protein were incubated with anti-Flag M2 agarose beads for 2 h at 4°C on a rotator. After extensive washing, proteins were eluted with 150 ng/ml of 3xFlag peptide by shaking for 30–40 min at 4°C. Proteins were then resolved by SDS-PAGE and stained for 2 h with Colloidal Coomassie Brilliant Blue (0.1% w/v Brilliant Blue G-250, 25% v/v methanol, 5% v/v acetic acid and milliQ water) for 1 h. Then,

destained with a Colloidal Destaining (7.5% v/v acetic acid, 5% v/v methanol and milliQ water). Finally, gel band was excised and assessed by mass spec (see below).

Western blot analysis

Cells were lysed in an appropriate volume of RIPA buffer (20 mM Tris-HCl pH 7.5, 150 mM NaCl, 1 mM EDTA, .5 mM sodium pyrophosphate - $\text{Na}_4\text{P}_2\text{O}_7$, 1 mM β -glycerophosphate - $\text{C}_3\text{H}_7\text{Na}_2\text{O}_6\text{P}$, 1 mM sodium orthovanadate - Na_3VO_4) containing 1% protease inhibitor cocktail (Sigma-Aldrich). Protein concentration was determined through the Pierce BCA Protein Assay Kit following manufacturer's instructions (Thermo Scientific) and 25 μg of each sample was prepared for SDS-PAGE with the addition of Sample buffer 4X. Electrophoresis was performed using ExpressPlus PAGE precast gels 4-20% (GeneScript), according to the manufacturer's instructions. After electrophoresis, protein samples were transferred to PVDF membranes (Bio-Rad) through a Trans-Blot TurboTM Transfer System (Bio-Rad) in semi-dry conditions, with the 1X Transfer Buffer (Bio-Rad) at 25 V for 20 min. Proteins were identified by the appropriate primary antibodies against: LRRK2 (Abcam #ab133474, 1:300), β -actin (Sigma-Aldrich #A1978, 1:10000), Annexin II (Genetex International #GTX101902, 1:200), Alpha-Synuclein (Abcam #ab138501, 1:10000), Flag M2-Peroxidase (Sigma-Aldrich #A8592, 1:10000); and then incubated for 1 h at RT with appropriate Horseradish-Peroxidase (HRP)-conjugated secondary antibodies (Invitrogen). The visualization of the signal was conducted using Immobilon Forte Western HRP Substrate (Millipore) and the VWR Imager Chemi Premium. Images were acquired in tiff format and processed by the ImageJ software to quantify total intensity of each single band.

Mass spectrometry analysis

364
365 Gel slices were cut into small pieces and subjected to reduction with dithiothreitol (DTT 10
366 mM in 50 mM NH_4HCO_3 , for 1 h at 56°C), alkylation with iodoacetamide (55 mM in 50 mM
367 NH_4HCO_3 , for 45 min at RT and in the dark) and finally to in-gel digestion with sequencing
368 grade modified trypsin (12.5 ng/ μL in 50 mM NH_4HCO_3 , Promega) as reported in [46].
369 Samples were analyzed using a LTQ-Orbitrap XL mass spectrometer (Thermo Fisher
370 Scientific) coupled to a HPLC Ultimate 3000 (Dionex – Thermo Fisher Scientific) through a
371 nanoSpray (NSI). Peptides were separated at a flow rate of 250 nL/min using a 11 cm long
372 capillary column (PicoFrit, 75 μm ID, 15 μm tip, New Objective) packed in house with C18
373 material (Aeris Peptide 3.6 μm XB C18; Phenomenex). A linear gradient of acetonitrile/0.1%
374 formic acid from 3% to 40% was used for peptide separation and the instrument operated in a
375 data dependent acquisition mode with a Top4 method (one full MS scan at 60000 resolution in
376 the Orbitrap, followed by the acquisition in the linear ion trap of the MS/MS spectra of the 4
377 most intense ions). Raw data files were analyzed using Proteome Discoverer 1.4 (Thermo
378 Fisher Scientific) connected to a Mascot local server (version 2.2.4, Matrix Science) and
379 searched against the human section of the Uniprot database (version July 2018, 95057 entries)
380 using the following parameters: trypsin was selected as digesting enzyme with up to one missed
381 cleavage allowed, precursor and fragment tolerance was set to 10 ppm and 0.6 Da respectively,
382 carbamidomethylation of cysteine residues was set as a fixed modification and methionine
383 oxidation as a variable modification. The precursor area ions detector node of Proteome
384 Discoverer was used to integrate the area of precursor ions. A search against a randomized
385 database and the algorithm Percolator were used to assess the false discovery rate (FDR) and
386 data were filtered to keep into account only proteins identified with at least two unique peptides
387 and a $\text{FDR} \leq 0.01$ both at peptide and protein level. Proteins were grouped into protein families
388 according to the principle of maximum parsimony.

Neutral red staining

Cells were plated in 24 wells plates (10×10^4 cells) and treated with α -syn PFFs (0.5 μ M, 24 h) once reached 80% of confluency with or without the autophagy inhibitor bafilomycin (50 nM, 1 h); at the end of the treatment, the cell culture medium was removed and OPTIMEM with a solution of 3-amino-7-dimethylamino-2-methyl-phenazine hydrochloride (Neutral red, Sigma-Aldrich) with a final concentration of 40 ng/ml, was added to the cells for 3-4 h. Cells were washed twice with DPBS and dissolved in a destaining solution composed of 50% ethanol, 49% deionized water, 1% glacial acetic acid and the absorbance was recorded by the use of a multi-well plate reader at the wavelength of 540 nm (Victor, Perkin Helmer). For each sample, treated and untreated, a replicate of two wells was used to determine protein concentration (BCA assay). Data were expressed as absorbance at 540 nm normalized to the absorbance recorded for the BCA assay and the final results in the graph were expressed as Neutral red staining absorbance in comparison with untreated controls.

Statistical analysis

Experiments were performed using cell cultures obtained either from embryos of at least three different pregnant mice or from at least three different groups of pups. H4 cells were used at the same *in vitro* passage number for the two independent experiments. Results are expressed as mean \pm standard error of the mean (SEM) or median with interquartile range; depending on whether data followed a Gaussian distribution or not. Gaussian distribution was assessed by D'Agostino & Pearson omnibus and Shapiro-Wilk normality tests. For Gaussian distribution, the statistical analysis between two groups was performed by unpaired Student's T-test. Data including more than two groups were analyzed by one-way ANOVA (Gaussian distribution) or Kruskal-Wallis test (non-Gaussian distribution) respectively followed by Tukey's multiple

412 comparisons test or Dunn's multiple comparisons test. Levels of significance were defined as
413 * $p \leq 0.05$ ** $p \leq 0.01$ *** $p \leq 0.001$. Statistical analysis was performed in Prism 6 (GraphPad).
414

Results

G2019S Lrrk2 astrocytes display impaired exogenous α -syn handling

To study how LRRK2 affects exogenous fibrillar α -syn clearance in astrocytes in total absence of microglia, we examined the uptake and degradation capacities of cortical stem cell-derived astrocytes isolated from *Lrrk2*^{-/-} and *Lrrk2*^{GS/GS} mice. As depicted in Figure 1A, astrocytes were exposed to 0.5 μ M α -syn PFFs for 24 h, thoroughly rinsed and then processed for analysis or incubated for additional six days in α -syn-free medium. TEM analysis verified the successful generation of PFFs and confirmed efficient sonication of α -syn PFFs used for the experiments (Figure 1B).

Comparable to our previous findings [8, 9, 32, 47], astrocytes engulfed and accumulated large amounts of α -syn (Figure 1C). All intracellular Cy3 α -syn deposits localized around the nucleus of astrocytes. Like reported by us before [32, 47], we observed different types of Cy3 α -syn inclusions: small dot-like inclusions and larger, cottony deposits (Figure 1C). The larger, more diffuse Cy3 α -syn inclusions were also found in close proximity to pyknotic cell nuclei (ingested by the astrocytes during the differentiation period and characterized by a condensed DAPI staining) (Figure 1C) [30, 32]. Moreover, immunocytochemistry revealed that ingested α -syn was deposited in vesicles expressing the endo-lysosomal marker Lamp-1 (Supplementary Figure 1) [8].

To study the different types of Cy3 α -syn inclusions more closely, z-stack imaging was performed. All Cy3 α -syn deposits were surrounded by or were observed in close proximity to GFAP staining (Figure 1D). GFAP is an intermediate filament protein that constitutes part of the cytoskeleton of astrocytes but does not encompass the whole cell (Supplementary Figure 2) [48]. GFAP staining thus underestimates the perimeter of astrocytes. Both small dot-like inclusions (Figure 1E, arrow head) and larger, cottony deposits (Figure 1E, arrow) were

observed and the ImageJ analysis macro used to quantify the amount of Cy3 α -syn inclusions was adaptable to analyze differently-sized Cy3 α -syn deposits separately (Figure 1E').

The quantification of all Cy3 α -syn particles together revealed that only *Lrrk2*^{GS/GS} astrocytes displayed a lower amount of α -syn inclusions (Supplementary Figure 3), a difference that predominantly resulted from the group of small α -syn deposits, as shown by quantifying the differently-sized inclusions separately (Figure 2A and B). Examining the small Cy3 α -syn deposits at the 24 h time-point, *Lrrk2*^{GS/GS} cells displayed lower values than *Lrrk2*^{+/+} for all parameters analyzed (Figure 2A, *Lrrk2*^{GS/GS} vs *Lrrk2*^{+/+} $p \leq 0.001$; Kruskal-Wallis test followed by Dunn's multiple comparisons test). *Lrrk2*^{GS/GS} also displayed lower Cy3 α -syn amounts compared to *Lrrk2*^{-/-} in terms of particle count ($p \leq 0.001$) and integrated density ($p \leq 0.05$), but not for the area measurement (Figure 2A; Kruskal-Wallis test followed by Dunn's multiple comparisons test). On the other hand, the analysis of larger Cy3 α -syn inclusions did not reveal any statistically significant differences between the LRRK2 genotypes (Figure 2B, Cy3 α -syn particle count: $p = 0.7268$, Cy3 α -syn area: $p = 0.0775$, Cy3 α -syn integrated density: $p = 0.0605$; Kruskal-Wallis test followed by Dunn's multiple comparisons test).

At the 24 h + 6 d time-point the only statistically significant difference observed for the small Cy3 α -syn particles was the integrated density measurement (Figure 2A, *Lrrk2*^{GS/GS} vs *Lrrk2*^{-/-} $p \leq 0.001$; Kruskal-Wallis test followed by Dunn's multiple comparisons test). For the large Cy3 α -syn inclusions no statistically significant difference between the LRRK2 genotypes was observed for all parameters analyzed at 24 h + 6 d (Figure 2B, Cy3 α -syn particle count: $p = 0.7689$, Cy3 α -syn area: $p = 0.8065$, Cy3 α -syn integrated density: $p = 0.5824$; Kruskal-Wallis test followed by Dunn's multiple comparisons test).

Insights on the degradation capacity of astrocytes were gained by observing changes between the two time-points (24 h vs 24 h + 6 d). Overall, we confirmed that astrocytes store rather than degrade the aggregated α -syn (Figure 2). Area and integrated density measurements showed a

1.5 to 2-fold increase for both small and large Cy3 α -syn deposits, while the number of particles counted did not change (apart for *Lrrk2*^{GS/GS}, which showed a 1.2-fold change increase of small Cy3 α -syn deposits). These results might be explained by the fact that aggregates are brought closer together over the six-day period. Following ingestion, the α -syn aggregates are relocated inside the cell to end up in “storage dumps” around the nucleus, a phenomenon that we have previously documented using different astrocytic culture systems after astrocytic engulfment of α -syn or amyloid-beta aggregates [9, 31].

Thus, our data indicate that the amount of α -syn present inside *Lrrk2*^{GS/GS} astrocytes is reduced compared to wild-type or *Lrrk2*^{-/-} astrocytes. The effect is normalized over time, suggesting that the pathogenic mutation influences the uptake rather than the degradation of α -syn.

G2019S striatal astrocytes show reduced engulfed α -syn

Given the high expression of LRRK2 in the striatum [10, 49, 50], we isolated striatal astrocytes from *Lrrk2*^{GS/GS}, *Lrrk2*^{-/-} and wild-type mice to further confirm our data. The culture purity was assessed by immunofluorescence against GFAP and Iba1, which are astrocytic and microglial markers, respectively (Supplementary Figure 4A-B). The characterization revealed that 94 \pm 2% of cells are identified as astrocytes and 7 \pm 2% of cells as microglia (Supplementary Figure 4A-B). Similar to cortical stem cell-derived astrocytes, striatal astrocytes are able to ingest and direct sonicated α -syn PFFs to endo-lysosomal organelles positive for Lamp2A marker (Supplementary Figure 4D).

To quantify *Lrrk2*-mediated effects of α -syn PFF clearance in this cellular system, we conjugated monomeric α -syn with a pH-sensitive dye named SNARF-1 C2-Maleimide (SNARF-1 from now on) followed by fibrillization and sonication. As shown by TEM analysis, SNARF conjugation does not affect α -syn PFF aggregation process (Figure 3A). Relevant for the experimental set up, we ruled out that the chemico-physical properties of the dye are

changed upon conjugation and fibrillation process (Supplementary Figure 5). Indeed, the inflection point of free and conjugated SNARF curves are 7.826 ($R=0.9956$) and 7.606 ($R=0.9918$), respectively (Supplementary Figure 5). SNARF is particularly suitable to sense pH that range between 6-9 (Supplementary Figure 5) [51, 52] allowing to monitor α -syn PFFs trafficking through the endo-lysosomal pathway. We treated cells with 0.5 μ M SNARF-labeled- α -syn PFFs and captured images after 24 h using live cell confocal microscopy at the two relevant emission ranges (Figure 3C). Quantification shows that *Lrrk2*^{GS/GS}, *Lrrk2*^{-/-} and wild-type striatal astrocytes display a similar cumulative distribution 550/630 ratio at the single particle level (Figure 3D). Therefore, in all the three genotypes SNARF-labelled- α -syn PFFs are distributed in overlapping organelle environments, excluding the possibility that LRRK2 interferes with the flux of extracellular α -syn once internalized as well as the global pH of the organelles. However, similar to what we observed in cortical astrocytes, the total particle number identified in the *Lrrk2*^{GS/GS} astrocytes (Figure 3D) as well as the number of particles per ROI are significantly reduced (Figure 3E, *Lrrk2*^{-/-} vs *Lrrk2*^{GS/GS} PFFs $p<0.001$ using Kruskal-Wallis test followed by Dunn's multiple comparisons test). Taken together, these results further support that the G2019S pathological mutation in *Lrrk2* modifies the ability of striatal astrocytes to intracellularly accumulate exogenous α -syn.

Lrrk2 impacts endo-lysosomal capacity in striatal astrocytes

Since the pathogenic mutation in *Lrrk2*^{GS/GS} astrocytes impairs their ability to store aggregated α -syn, we next sought to examine the functional aspects of the endo-lysosomal pathway. First, we investigated whether *Lrrk2* has an impact on the number and dimension of endo-lysosomal structures in mouse striatal astrocytes. Astrocytes from *Lrrk2*^{+/+}, *Lrrk2*^{-/-} and *Lrrk2*^{GS/GS} mice were imaged by TEM and the number and area of lysosomal-like structures were measured (Figure 4A-C). Quantification showed that both *Lrrk2* ablation and the G2019S pathological mutation caused a significant decrease in the number of lysosomal-like structures in astrocytic

514 cells (Figure 4A-B; *Lrrk2*^{+/+} vs *Lrrk2*^{-/-} p<0.001, *Lrrk2*^{+/+} vs *Lrrk2*^{GS/GS} p<0.001, *Lrrk2*^{GS/GS} vs
 515 *Lrrk2*^{-/-} p>0.05.; Kruskal-Wallis test followed by Dunn's multiple comparisons test) and in the
 516 intact striatum (Supplementary Figure 6A-B; *Lrrk2*^{+/+} vs *Lrrk2*^{-/-} p<0.05, unpaired T-test).
 517 However, the absence of *Lrrk2* showed enlarged structures, compared to *Lrrk2*^{+/+} as well as
 518 *Lrrk2*^{GS/GS} astrocytes (Figure 4A-C; *Lrrk2*^{+/+} vs *Lrrk2*^{-/-} p<0.001, *Lrrk2*^{+/+} vs *Lrrk2*^{GS/GS} p>0.05,
 519 *Lrrk2*^{GS/GS} vs *Lrrk2*^{-/-} p<0.001, Kruskal-Wallis test followed by Dunn's multiple comparisons
 520 test). *Lrrk2*^{+/+} and *Lrrk2*^{-/-} astrocytes have similar overall volume occupied by lysosomal
 521 structures calculated as mean lysosomal number x mean lysosome volume (1.7 and 2.0
 522 $\mu\text{m}^3/\text{mm}^2$). However, *Lrrk2*^{GS/GS} astrocytes showed half of the lysosomal global volume (1.0
 523 $\mu\text{m}^3/\text{mm}^2$) compared to *Lrrk2*^{+/+} and *Lrrk2*^{-/-} astrocytes. To confirm our data, we analyzed the
 524 astrocytic endo-lysosomal compartment by immunofluorescence using Lamp2A as a marker of
 525 late endosomes/lysosomes. Also with this approach we revealed a significant reduction of the
 526 organelle number in *Lrrk2*^{-/-} and *Lrrk2*^{GS/GS} astrocytes (Figure 4D-E; *Lrrk2*^{+/+} vs *Lrrk2*^{-/-}
 527 p<0.001, *Lrrk2*^{+/+} vs *Lrrk2*^{GS/GS} p<0.001, *Lrrk2*^{GS/GS} vs *Lrrk2*^{-/-} p<0.01, One-way ANOVA
 528 Tukey's multiple comparison test) associated with organelle enlargement in the *Lrrk2*^{-/-} cells
 529 (Figure 4D-F; *Lrrk2*^{+/+} vs *Lrrk2*^{-/-} p<0.001, *Lrrk2*^{+/+} vs *Lrrk2*^{GS/GS} p<0.001, *Lrrk2*^{GS/GS} vs *Lrrk2*^{-/-}
 530 ^{-/-} p<0.001, Kruskal-Wallis test followed by Dunn's multiple comparisons test).
 531 Next, the activation of the endo-lysosomal pathway was assessed in α -syn PFF-treated striatal
 532 astrocytes and untreated control cells by applying the neutral red assay. Neutral red is a dye that
 533 is specifically retained by acidic vesicles [53] and it is frequently used as reliable indicator of
 534 phagocytic activity [54, 55]. As expected, bafilomycin dissipates endo-lysosomal pH markedly
 535 decreasing Neutral red accumulation in all experimental conditions (Figure 4G). In contrast,
 536 Neutral red staining is detected in cells in the absence of bafilomycin treatment by measuring
 537 absorbance at 540 nm in cell lysates. We did not report any statistical difference between the
 538 three genotypes in absence of α -syn PFFs (under untreated condition) (Figure 4G). However,

PFFs-stimulation induced increase of Neutral red staining in astrocytes, indicating that phagocytosis efficiently occurs in *Lrrk2*^{+/+} and *Lrrk2*^{-/-} astrocytes but not in *Lrrk2*^{GS/GS} cells (Figure 4G, *Lrrk2*^{+/+} vs *Lrrk2*^{+/+} PFFs $p < 0.001$; *Lrrk2*^{-/-} vs *Lrrk2*^{-/-} PFFs $p < 0.001$; *Lrrk2*^{GS/GS} vs *Lrrk2*^{GS/GS} PFFs $p < 0.05$; One-way ANOVA Tukey's multiple comparison test).

Collectively, these observations suggest that the G2019S mutation influences morphology and number of the endo-lysosomal vesicles. Thus, the overall lysosomal degradation capacity appeared reduced in the presence of G2019S pathological mutation.

LRRK2 interacts with ANXA2

To identify LRRK2-specific effectors of astrocyte-mediated α -syn PFF clearance using an unbiased approach, we performed a high-throughput screening of candidate protein-protein interaction (PPI) partners via affinity purification (AP) coupled with tandem mass spectrometry. Specifically, we processed LRRK2-immunoprecipitated binders by liquid chromatography mass spectrometry (LC-MS) from H4 cells (Figure 5A). LRRK2 was immunopurified using anti-Flag agarose beads and eluted from the resin to exclude contaminants with high affinity for the resin. With this analysis, we compared LRRK2 interactome in PFF-treated and untreated samples. In Figure 5B, we show the LRRK2 immunopurification steps in the two conditions. For each interactor, we calculated the ratio between the chromatographic area relative to the peptides belonging to the proteins detected in treated versus non-treated conditions. The value was normalized by the peak area of immunoprecipitated LRRK2 in the two experimental conditions and reported in Figure 5C. Out of the mass spectrometry hits, found in two independent replicates, AnnexinA2 (human ANXA2) increased its affinity for LRRK2 upon α -syn PFF treatment. Intriguingly, ANXA2 is a phospholipid-binding protein that intervenes in phagocytic processes at multiple levels [56-

62]. Specifically, it was reported that *AnxA2* deficits are linked to a decreased endocytosis and particle internalization [56, 63, 64]. Based on this functional relevance, we validated the role of ANXA2 in regulating exogenous fibrillar α -syn internalization. In H4 astrocytic cells, GFP-transfected ANXA2 diffusely distributed throughout the cytoplasm under untreated condition but partially re-localized around the α -syn fibrils upon treatment (Supplementary Figure 7). Moreover, internalized α -syn fibrils were found to be surrounded by ANXA2 within the cell (Figure 5D). As reported for ectopically expressed GFP-ANXA2 in H4 cells (Figure 5D), endogenous mouse astrocytic *AnxA2* localizes into subcellular puncta in the near proximity of internalized PFF particles (Figure 6A). To evaluate the involvement of mouse *AnxA2* in astrocyte-mediated α -syn PFF phagocytic clearance at the endogenous level, we acutely downregulated *AnxA2* in primary striatal astrocytes using siRNA. Around the 60% of *AnxA2* downregulation was achieved in *AnxA2* siRNA-transfected astrocytes compared to controls (Supplementary Figure 8A-C). *AnxA2* downregulation did not significantly affect the LRRK2 protein level in transfected astrocytes (Supplementary Figure 8A-B). To image siRNA recipient cells, we co-transfected primary striatal astrocytes with *AnxA2* siRNA and a GFP-encoding plasmid. As represented in Figure 6B, we acquired images upon 24h of PFF treatment. To quantify the number of α -syn inclusions in the two conditions, GFP-positive cells were analyzed using ImageJ. Quantification of internalized α -syn-positive puncta shows that *AnxA2* downregulation decreases the amount of intracellular deposits per cell compared to scramble transfected controls (Figure 6C-D; $p < 0.001$, Kruskal-Wallis test followed by Dunn's multiple comparisons test). To validate our findings, we also evaluated intracellular α -syn PFFs by western blot analysis upon *AnxA2* downregulation (Figure 6E). As already shown in Supplementary Figure 8, siRNA transfection in primary striatal astrocytes does not affect LRRK2 protein level, neither in treated nor untreated conditions (Figure 6E-F). Again, *AnxA2* downregulation was successfully achieved and maintained after PFF treatment (Figure 6E-G;

scramble siRNA vs *AnxA2* siRNA +/- PFFs $p<0.001$; scramble siRNA + PFFs vs *AnxA2* siRNA +/- PFFs $p<0.001$; one-way ANOVA followed by Tukey's multiple comparisons test). A slight but significantly decreased level of AnxA2 was also revealed upon PFF exposure in the scramble siRNA astrocytes (Figure 6E-G; scramble siRNA vs scramble siRNA + PFFs $p<0.01$; one-way ANOVA followed by Tukey's multiple comparisons test). However, our results showed that the amount of accumulated α -syn significantly decreased by comparing lysates obtained from *AnxA2* siRNA transfected astrocytes versus control (Figure 6E-H; scramble siRNA + PFFs vs *AnxA2* siRNA + PFFs $p<0.01$, Unpaired T-test). Overall, these findings suggest a functional link between *Lrrk2* and AnxA2 in astrocyte-mediated exogenous α -syn clearance and that *AnxA2* deficits influence the astrocytic ability to store α -syn aggregates.

G2019S Lrrk2 striatal astrocytes display AnxA2 deficits

To determine whether *Lrrk2* impacts α -syn PFF clearance through AnxA2, we measured AnxA2 protein content in treated versus untreated striatal primary astrocytes. Here, we focused our analysis on *Lrrk2*^{+/+} versus *Lrrk2*^{GS/GS} genotype. Cell lysates from cultured striatal astrocytes were subjected to western blot and AnxA2 endogenous expression was assayed. As shown in Figure 7A, AnxA2 level is significantly decreased in *Lrrk2*^{GS/GS} astrocytes both under basal and treated conditions compared to wild-type cells (Figure 7A-C; *Lrrk2*^{+/+} vs *Lrrk2*^{GS/GS} +/- PFFs $p<0.05$, One-way ANOVA Tukey's multiple comparison test). In agreement with our data reported in Figure 6, AnxA2 down-regulation in G2019S *Lrrk2*^{GS/GS} astrocytes is associated with a significant decrease in intracellular α -syn deposits (Figure 7A-D; *Lrrk2*^{+/+} + PFFs vs *Lrrk2*^{GS/GS} + PFFs $p<0.05$; Unpaired T-test). However, the LRRK2 protein level was not affected in *Lrrk2*^{GS/GS} astrocytes in neither treated nor untreated conditions (Figure 7A-B). We then evaluated AnxA2 localization under basal condition and upon α -syn PFFs treatment in *Lrrk2*^{GS/GS} astrocytes, compared to control astrocytes (Figure 7 E). As already reported by

others [57] and shown here for H4 astrocytic cells, ANXA2 is homogenously distributed within the cytoplasm under basal conditions, but accumulates into discrete puncta upon stimuli. Using ImageJ, we quantified ANXA2 fluorescent positive puncta in control and α -syn PFF exposed astrocytes of the two genotypes. Our results show that ANXA2 re-localization takes place in both *Lrrk2*^{+/+} and *Lrrk2*^{GS/GS} astrocytes, while it appeared significantly decreased in cells harboring the pathogenic mutation (Figure 7F, *Lrrk2*^{+/+} vs *Lrrk2*^{+/+} PFFs $p < 0.001$, *Lrrk2*^{GS/GS} vs *Lrrk2*^{GS/GS} PFFs $p < 0.01$; *Lrrk2*^{+/+} + PFFs vs *Lrrk2*^{GS/GS} + PFFs $p < 0.001$; Kruskal-Wallis test followed by Dunn's multiple comparisons test). We then quantified α -syn deposits associated with ANXA2 puncta within each cell by measuring particles proximity using ImageJ. We observed that less α -syn intracellular inclusions are found in close proximity to ANXA2 in *Lrrk2*^{GS/GS} striatal astrocytes compared to *Lrrk2*^{+/+} controls (Figure 7E and G, *Lrrk2*^{+/+} vs *Lrrk2*^{GS/GS} $p < 0.001$; unpaired T-test).

Overall, our results show that the ANXA2 level is diminished in *Lrrk2*^{GS/GS} astrocytes and this phenomenon is associated with a decrease number of intracellular α -syn deposits.

Discussion

Aggregated α -syn is the main constituent of the intra-neuronal and intra-glial proteinaceous inclusions found in PD [4, 7]. Compelling evidence suggests that cell-to-cell transmission of the α -syn aggregates results in the anatomical spread of the disease [65-71]. The intercellular transfer can occur through different mechanisms, including tunneling nanotubes, exosomes and secretion of free pathological α -syn aggregates [9, 69, 72-74]. Following secretion, α -syn aggregates are sequestered from the extracellular space by neighboring cells [69-71, 74-76]. Astrocytes, which are the major glial cell type, are known to ingest particularly large amounts of aggregated α -syn that are then intracellularly stored, rather than degraded [9, 32]. We have previously shown that the accumulation of aggregated α -syn in human astrocytes disrupts their lysosomal machinery, induces cell-to-cell transfer between astrocytes and promote T-cell

activation [8, 9]. However, the exact role of astrocytes in PD and the particular molecular mechanisms that impact on their clearing capacity remain elusive. In the last few years, several reports have suggested that pathogenic and functional mutations in LRRK2 influence the biology of human and murine astrocytes at multiple levels both *in vivo* and *in vitro* [24, 77-81]. In addition, LRRK2 is emerging as a key player in the clearance of extracellular particles in macrophages and monocytes, with its involvement both in internalization step and downstream in vesicle maturation and sorting [22-24, 26, 27]. However, no investigation has focused on the role of LRRK2 in astrocyte-mediated α -syn clearance.

We started our investigation by studying the effect of *Lrrk2* in α -syn clearance over time thus selecting a mouse model that lacks microglia contamination [29, 37-39]. Our study revealed that the most common pathogenic mutation in LRRK2, G2019S, negatively regulates the amount of engulfed fibrillar α -syn in astrocytes. In agreement with our evidence, it has recently been proposed that LRRK2 kinase activity blocks micropinocytosis in phagocytes through the phosphorylation of Rab10 [27]. Analyzing the differently sized α -syn inclusions separately revealed that the reduced α -syn accumulation in *Lrrk2*^{GS/GS} astrocytes was predominantly driven by the small α -syn inclusions. However, this effect normalized over time and could be explained by the attempt of astrocytes to degrade the engulfed material, but being inefficient they rather store the ingested α -syn, which we have also seen in previous studies [9, 32]. Indeed, the amount of accumulated α -syn six days after the exposure to α -syn PFFs increased in all three genotypes, with a more pronounced effect observed in presence of the pathological mutation. This increase cannot be attributed to more α -syn being taken up by the astrocytes, since the cells were rinsed extensively after the 24h exposure to α -syn PFFs. Instead, the reason for the increase was redistribution of α -syn aggregates inside the cell. Over the six days, the intracellular α -syn deposits are brought closer together in the region around the nucleus, which results in larger

inclusions with stronger fluorescence signal. The larger area measurements in combination with an unchanged particle count, indicates the formation of bigger aggregates overall. Also, α -syn particles, previously below detection limit, may have clustered and thus become detectable at the later time-point.

In the neural stem cell-based astrocyte model, apoptotic cells are naturally produced during the differentiation phase, which are engulfed and stored by the astrocytes. The reason why pyknotic cell nuclei and large α -syn deposits appear in close proximity inside the astrocytes is that the cells direct the ingested material to the same cellular compartments, or “storage dumps”. This is a phenomenon that we have previously demonstrated, in different astrocytic culture systems, following α -syn or amyloid-beta exposure [9, 31]. Although, the storage of cell corpses and protein aggregates is stressful for the astrocytes, the number of viable astrocytes during the experimental timeframe has been shown to remain constant [31]. We have previously observed that engulfed α -syn oligomers and the lysosomal marker Lamp-1 only temporarily co-localize [9, 32]. Thus, the persisting α -syn deposits could be a sign for an overwhelmed degradation system, which has been shown to result in cytoplasmic aggregates known as aggresomes as well as inclusion bodies [82]. This suggests that astrocytes try to degrade the engulfed α -syn, but in the end fail to do so and rather store and to some extent transfer the engulfed material to neighboring astrocytes.

Astrocytes that populate the striatum are relevant to PD pathology since they are in close proximity to dopaminergic terminals of the SNpc and it is unknown how they respond to neuronal-released α -syn. Here, we confirmed that the G2019S pathogenic mutation in *Lrrk2* reduces the amount of internalized α -syn in primary mouse striatal astrocytes without impairing the flow of particles through the endo-lysosomal system. However, *Lrrk2* pronouncedly

689 changes the architecture of the late-endosome/lysosomal organelles in striatal astrocytes. By
690 TEM, we showed that the genetic ablation of *Lrrk2* causes an enlargement of lysosomal
691 structures in primary striatal astrocytes. This finding is in agreement with several other
692 published observations of kidney and lung tissues [20, 83]. The change in lysosomal size was
693 however compensated by an overall decrease in lysosomal structures, as shown for both *Lrrk2*^{-/-}
694 primary striatal astrocytes and for astrocytes in *Lrrk2*^{-/-} striatum brain sections. A similar trend
695 has been observed by measuring Lamp2A endo-lysosomal positive-structures. The pathogenic
696 G2019S mutation in *Lrrk2* induces an endo-lysosomal shrinkage associated with a decreased
697 number of organelles in primary striatal astrocytes, both when quantifying lysosomal-like
698 structures with TEM and Lamp2A-positive structures using confocal imaging. Similar
699 morphological data has been observed in G2019S PD patient-specific human neuroepithelial
700 stem cells and in primary cortical neurons from *Lrrk2*^{GS/GS} mice, using close or identical
701 experimental settings [19, 84]. In contrast to the above findings, Henry et al., 2015 indicated
702 enlarged lysosomes in cultured cortical astrocytes overexpressing G2019S human LRRK2
703 compared to wild-type astrocytes, without discriminating between the contribution of the
704 pathogenic mutation and the LRRK2 level [12]. The overall volume occupied by lysosomal-
705 like structures indicated that striatal *Lrrk2*^{GS/GS} but not *Lrrk2*^{-/-} astrocytes present an intrinsic,
706 basal deficit in the endo-lysosomal holding capacity (half total volume) with respect to the wild-
707 type counterpart. Contrary to our imaging results, we did not detect any differences between
708 genotypes by labeling acidic vesicles with Neural red solution at basal level, suggesting that a
709 bulk approach might not be sufficiently sensitive. However, astrocytes displayed an increased
710 staining of the acidic compartment using Neutral red solution after 24 h of PFF treatment, in
711 agreement with an enhanced phagocytic activity. *Lrrk2*^{GS/GS} cells did not show any
712 intensification of Neural red staining suggesting a possible impairment in their ability to ingest
713 extracellular α -syn. In phagocytes, it was recently reported that the endo-lysosomal

compartment undergoes adaptation, remodeling and expansion during particle internalization through an enhanced translation [85]. In this regard, our findings might suggest that striatal astrocytes harboring the G2019S mutation in *Lrrk2* also fail to adapt and expand their endo-lysosomal system when they are stimulated to phagocytize, resulting in α -syn-defective internalization.

For the first time, our study identifies ANXA2 as a novel player in α -syn clearance in astrocytic cells. ANXA2 is an actin-binding protein that modulates many intracellular trafficking events, via the regulation of actin polymerization dynamics. Specifically, ANXA2 is recruited to the plasma membrane, during the formation of the phagocytic cup [56], and assists endosomes upon particle internalization by preventing destabilization [57]. Of note, several papers reported the involvement of ANXA2 in autophagy [58-61], a degradative process highly interconnected with the clearance of pathogens and aggregated proteins, including α -syn [62]. Indeed, multiple line of evidence indicates that *AnxA2* knockdown or knock-out prevents endocytic transport beyond early endosomes, interferes with particle phagocytic transport and causes endosomal ultrastructural impairments [56, 86, 87]. Relevant for diseases associated with accumulation of aggregated proteins, ANXA2 expression is enhanced at the cell periphery in reactive astrocytes positioned in close proximity to senile plaques and degenerating neurons of Alzheimer's disease human *post mortem* brains [88]. This immunohistological data suggest that ANXA2 might be important for the clearance of extracellular toxic proteinaceous material. Indeed, we demonstrated that endogenous *AnxA2* downregulation negatively impacts exogenous α -syn clearance in primary striatal astrocytes as shown by decreased amount of intracellular α -syn deposits as well as unfolded α -syn in the lysates. Of note, ANXA2 enhanced its affinity for LRRK2 upon α -syn PFFs treatment in astrocytic-like cells pointing to a functional interaction between the two proteins. Astrocytes expressing pathogenic *Lrrk2* displayed a significant

AnxA2 deficit at protein level followed by a reduction in intracellular α -syn positive puncta and α -syn in the lysates. Endogenous AnxA2 in *Lrrk2*^{GS/GS} astrocytes has impaired ability to regulate i) intracellular re-localization into puncta and ii) proximity to internalized α -syn particles. AnxA2 downregulation can also explain the endo-lysosomal shrinkage showed in *Lrrk2*^{GS/GS} astrocytes. How LRRK2 regulates the ANXA2 level in astrocytes and the impact of the G2019S mutation in this process needs to be explored in the future. Aggregated α -syn is engulfed by cells by different molecular processes, including receptor-mediated endocytosis and phagocytosis that probably differ according to particle dimension as well as cell type [89-91]. Our study reveals that the pathogenic G2019S mutation primarily affects the clearance of exogenous small α -syn inclusions, possibly by reducing internalization rather than enhancing degradation. In this regard, future studies will be dedicated to the study of the molecular mechanism of PFF handling mediated by ANXA2.

Conclusions

Being the most numerous glial cell type in the central nervous system, astrocytes have great impact on brain homeostasis. Recently, it has been shown that they uptake exogenous fibrillar α -syn. Yet, their exact role in PD pathology remains elusive. In the present study, we identify astrocytes as a possible player in LRRK2-mediated PD pathology. Taken together, our results demonstrate that LRRK2 impacts on astrocyte-mediated α -syn clearance. Astrocytes harboring the most common pathogenic PD-linked mutation G2019S in *Lrrk2* display a reduction of internalized α -syn as well as an impairment of their endo-lysosomal capacity. This impairment is associated with deficits in the amount of AnxA2, a novel protein shown to be involved in the clearance process. Aberrant mechanisms of astrocyte-mediated α -syn clearance might contribute to neuronal-released α -syn stagnation in the extracellular space thus enhancing toxicity. Our data offer a better understanding of the molecular mechanism behind impaired α -

syn clearance in G2019S astrocytes and highlight astrocytes as a promising therapeutic target in the context of LRRK2-mediated PD.

Figure legends

Figure 1 Accumulation of aggregated α -syn in *Lrrk2* astrocytes. **A)** Schematic outline of the experimental set-up. Cells were exposed to 0.5 μ M sonicated Cy3 α -syn PFFs for 24 h. **B)** TEM images of α -syn PFFs pre and post sonication. Scale bars 1 μ m. **C)** Representative fluorescence microscopy images of *Lrrk1*^{+/+}, *Lrrk2*^{-/-} and *Lrrk2*^{GS/GS} astrocytes (GFAP, green) at 24 h; cell nuclei stained with DAPI (blue) and α -syn labeled with Cy3 (red). Insets show a close-up of Cy3 α -syn inclusions. **D)** Orthogonal projections of z-stack images taken with a fluorescence microscope: main view (x/y), top (x/z) and right (y/z). Projections were made along the lines depicted in the main image. Astrocytes (GFAP, green), Cy3 labeled α -syn (red), DAPI (blue). **E)** Fluorescence microscopy image showing the differently sized Cy3 α -syn inclusions observed: small dot-like inclusions (arrow head) and larger, cottony deposits (arrow). **E')** Displays of the particle count obtained from the ImageJ analysis when including either all Cy3 α -syn deposits or only the small Cy3 α -syn inclusions. Scale bars = 20 μ m (C, D and E).

Figure 2 Analysis of the differently sized α -syn inclusions in *Lrrk2* astrocytes. **A** and **B)** Analysis of small and large Cy3 α -syn inclusions, respectively. Quantifications of Cy3 α -syn particle count, total area and integrated density were performed using ImageJ. For both time-points ten images per independent cell culture (24 h: *Lrrk1*^{+/+} n = 7, *Lrrk2*^{-/-} n = 6 and *Lrrk2*^{GS/GS} n = 5; 24 h + 6 d: *Lrrk1*^{+/+} n = 6, *Lrrk2*^{-/-} n = 6 and *Lrrk2*^{GS/GS} n = 5) were analyzed and reported. For each time-point, the statistical analysis was performed with the Kruskal-Wallis test followed by Dunn's multiple comparisons test, since the data did not follow Gaussian distribution for all groups. * $p \leq 0.05$ ** $p \leq 0.01$ *** $p \leq 0.001$

Figure 3 Internalization of aggregated α -syn in striatal astrocytes. **A)** TEM images of SNARF-1 α -syn PFFs pre and post sonication. **B)** Schematic outline of the experimental set-up. Cells were exposed to 0.5 μ M sonicated SNARF-1 α -syn PFFs for 24 h and imaged using live confocal laser scanning microscopy. **C)** Representative images of primary *Lrrk2*^{+/+} striatal astrocytes treated with SNARF-1 α -syn PFFs were acquired at range of 530-550 and 610-630 nm. Scale bar 50 μ m. **D and E)** Eight images per cell culture were analyzed (n=4 independent cultures). For each image, ROIs were traced and quantification of α -syn single-particle 550/630 ratio (IntDen) and number were performed using ImageJ. The cumulative distribution of the single-particle ratio was graphed for each genotype in **D** and particle number per ROI in **E**. Statistical analysis in **E** was performed using Kruskal-Wallis test followed by Dunn's multiple comparisons test. * $p \leq 0.05$ ** $p \leq 0.01$ *** $p \leq 0.001$

Figure 4 Description of the endo-lysosomal pathway in *Lrrk2* striatal astrocytes.

A) Representative TEM image of primary striatal astrocyte section containing electron dense lysosomal-like structures (arrows). Scale bar 2 μ m. **B and C)** Forty TEM images were acquired from n=4 per genotype. Each cell was imaged by covering the entire cytoplasm and lysosomal-like structure number and area were measured using ImageJ. **D)** Representative image of the staining using Lamp2A (green) as a marker for the endo-lysosomal pathway, DAPI (blue) for the nuclei and F-actin (cyano) to define cells. Scale bar 20 μ m. Inset shows a close-up of Lamp2A-positive structures. **E and F)** Four images per cell culture were analyzed (n=3 per genotype). **G)** Neutral red assay was performed in primary striatal astrocytes from the three genotypes upon unlabeled α -syn PPF treatment (n=4 per genotype). Bafilomycin has been applied as negative control. Absorbance at 540 nm measured upon cell lysates was normalized by total protein content. Quantifications of Lamp2A-positive structure number and area were analyzed using ImageJ. Statistical analysis in **B**, **C** and **F** was made by Kruskal-Wallis test followed by Dunn's multiple

comparisons test. Statistical analysis in **E** and **G** was performed with one-way ANOVA followed by Tukey's multiple comparisons test. * $p \leq 0.05$ ** $p \leq 0.01$ *** $p \leq 0.001$

Figure 5 Characterization of LRRK2 interactome in stimulated condition. **A)** Schematic outline of the experimental set-up. H4 cells were transfected using 3xFlag-LRRK2 encoding plasmid and, after 48 h post transfection, treated with 0.5 μ M sonicated unlabeled α -syn PFFs for 24 h. LRRK2 was subsequently immunopurified using anti-Flag agarose beads (IP), eluted with Flag peptide (elution) and subjected to LC-MS/MS analysis. FT: flow-through, unbound LRRK2. **B)** Western blot analysis showing LRRK2 expression, immuno-purification and elution in H4 cells in treated and basal conditions. **C)** Relative quantification of LRRK2 interactome under treated and untreated conditions. The area of the precursor ions identified by LC-MS/MS analysis was used as a quantitative measure of the protein content. The ratio between the area of the precursor ions of untreated and treated samples (normalized by the content of LRRK2) was then considered to highlight proteins showing a different affinity for LRRK2 in the two conditions (n=2). **D)** H4 cells transfected with GFP-ANXA2 in α -syn PFF-treated condition verifying the proximity of internalized α -syn fibrils and transfected AnxA2. AnxA2-GFP (green), α -syn (red), DAPI (blue). Scale bar 30 μ m.

Figure 6 Investigation of AnxA2 function in astrocyte-mediated α -syn phagocytic clearance. **A)** Unlabeled α -syn PFFs have been applied to primary astrocytes for 24 h. Projections verify the proximity of the internalized α -syn fibrils and endogenous AnxA2. Cell cytoskeleton (F-actin, cyano), α -syn (red), AnxA2 (green), DAPI (blue). Scale bar 20 μ m. **B)** Schematic outline of the experimental set-up. Cells were transfected using 3xFlag-GFP encoding plasmid together with scramble or AnxA2 siRNA. 48 h post transfection cells were treated with 0.5 μ M sonicated α syn PFFs for 24 h and imaged using

837 confocal microscopy. **C)** Representative images of primary striatal astrocytes transfected
838 with scramble or Anxa2 siRNA together with a GFP-encoding plasmid in α -syn PFF-
839 treated condition. Projections verify the proximity of the internalized α -syn fibrils; GFP
840 (green), α -syn (red), DAPI (blue). Scale bar 30 μ m. **D)** Four images per cell culture were
841 analyzed (n=3). Quantifications of α -syn PFFs fluorescent positive puncta were performed
842 using ImageJ (ComDet plugin). **E)** Western blot analysis of primary striatal astrocyte
843 lysates transfected with scramble and AnxA2 siRNA under basal and PFF-treated
844 conditions. Anti-Lrrk2, anti- α -syn and anti-AnxA2 antibodies have been employed. **F, G**
845 and **H)** Quantification of band intensity was performed using ImageJ and normalized by β -
846 actin (n=3). Statistical analysis in **D** was made by Kruskal-Wallis test followed by Dunn's
847 multiple comparisons test. Statistical analysis in **F, G and H** was performed with an
848 unpaired t-test or one-way ANOVA followed by Tukey's multiple comparisons test. * $p \leq$
849 0.05 ** $p \leq 0.01$ *** $p \leq 0.001$

850 **Figure 7** Analysis of AnxA2 function in G2019S primary striatal astrocytes at endogenous
851 level. **A)** Western blot analysis of primary striatal astrocyte lysates under PFF-treated and
852 basal conditions using anti-Lrrk2, anti- α -syn and anti-AnxA2 antibodies. **B, C and**
853 **D)** Quantification of band intensity was performed using ImageJ and normalized by β -actin
854 (n=4). **E)** Representative images of *Lrrk2*^{+/+} and *Lrrk2*^{GS/GS} astrocytes treated or not with
855 α -syn PFFs and stained with anti-AnxA2 (green), anti- α -syn (red), F-actin (cyano) and cell
856 nuclei with DAPI (blue). Scale bar 20 μ m. Insets show a close-up of α -syn inclusions and
857 re-localized AnxA2. **F and G)** Eight images per cell culture were analyzed (n=3).
858 Quantifications of Anxa2 puncta and AnxA2- α -syn PFFs proximity were performed using
859 ImageJ. Statistical analysis in **F and G** was made by Kruskal-Wallis test followed by
860 Dunn's multiple comparisons test. Statistical analysis in **B, C and D** was performed with

861 unpaired t-test or one-way ANOVA followed by Tukey's multiple comparisons test.

862 * $p \leq 0.05$ ** $p \leq 0.01$ *** $p \leq 0.001$

863 **Additional materials**

864 File name: Additional file 1 - supplementary figures (.pdf)

865 In the attached file Supplementary figures (1-6) are provided.

866

867	List of abbreviations	
868	AnxA2	Annexin A2
869	AP	Affinity Purification
870	α -syn	Alpha-Synuclein
871	bFGF	basic Fibroblast Growth Factor
872	BME	Basal Medium Eagle
873	BSA	Bovine Serum Albumin
874	DMEM	Dulbecco's Modified Eagle Medium
875	DPBS	Dulbecco's Phosphate Buffered Saline
876	DTT	Dithiothreitol
877	EGF	Epidermal Growth Factor
878	FBS	Fetal Bovine Serum
879	FDR	False Discovery Rate
880	GFAP	Glial Fibrillary Acidic Protein
881	HRP	Horseradish-Peroxidase
882	LAMP	Lysosome-Associated Protein
883	LC-MS	Liquid Chromatography Mass Spectrometry
884	LRRK2	Leucine Rich Repeat Kinase 2
885	NGS	Normal Goat Serum
886	PD	Parkinson's disease
887	PEI	Polyethylenimine
888	PFA	Paraformaldehyde
889	PFFs	Pre-Formed Fibrils
890	PPI	Protein-Protein Interaction
891	ROI	Region of Interest

892 RT Room Temperature
893 TEM Transmission Electron Microscopy

894

895 **Declarations**

896 *Ethics approval and consent to participate*

897 All animal procedures were approved by the Ethical Committee of the University of Padova
898 and the Italian Ministry of Health (license 46/2012 and 105/2019).

899

900 *Consent for publication*

901 Not applicable.

902

903 *Availability of data and materials*

904 All data generated or analyzed during this study are included in this article.

905

906 *Competing interests*

907 The authors declare that they have no competing interests.

908

909 *Funding*

910 This study was supported by grants from the University of Padova, the Italian Ministry of
911 Health, Swedish Research Council, the Swedish Parkinson Foundation, Åhlén Foundation, the
912 Dementia Association Foundation, Olle Engkvist Foundation, Torsten Söderbergs Foundation
913 and the Swedish Brain Foundation. MET is a Tier 2 Canada Research Chair in *Neurobiology*
914 *of Aging and Cognition*.

915

916 *Authors' contributions*

LS-G designed the study, optimized and performed experiments, interpreted data and wrote the manuscript; VG designed the study, optimized and performed experiments, interpreted data and wrote the manuscript; LI prepared astrocyte primary cultures; IB and GA performed mass spec experiments; AM, MS and IT produced PFFs; NP and EG contributed to data analysis; EG, MET, LB have contributed to manuscript editing and optimization; AE designed the study, interpreted data and wrote the manuscript; LC designed the study, interpreted data and wrote the manuscript. All authors have read and approved the final manuscript.

Acknowledgements

We are grateful to Prof. Chiara Romualdi at UniPD for the statistical advices.

References

1. Jankovic J: **Parkinson's disease: clinical features and diagnosis.** *J Neurol Neurosurg Psychiatry* 2008, **79**:368-376.
2. Spillantini MG, Schmidt ML, Lee VM, Trojanowski JQ, Jakes R, Goedert M: **Alpha-synuclein in Lewy bodies.** *Nature* 1997, **388**:839-840.
3. Tu PH, Galvin JE, Baba M, Giasson B, Tomita T, Leight S, Nakajo S, Iwatsubo T, Trojanowski JQ, Lee VM: **Glial cytoplasmic inclusions in white matter oligodendrocytes of multiple system atrophy brains contain insoluble alpha-synuclein.** *Ann Neurol* 1998, **44**:415-422.
4. Wakabayashi K, Hayashi S, Yoshimoto M, Kudo H, Takahashi H: **NACP/alpha-synuclein-positive filamentous inclusions in astrocytes and oligodendrocytes of Parkinson's disease brains.** *Acta Neuropathol* 2000, **99**:14-20.

- 941 5. Terada S, Ishizu H, Yokota O, Tsuchiya K, Nakashima H, Ishihara T, Fujita D, Ueda
942 K, Ikeda K, Kuroda S: **Glial involvement in diffuse Lewy body disease.** *Acta*
943 *Neuropathol* 2003, **105**:163-169.
- 944 6. Croisier E, Graeber MB: **Glial degeneration and reactive gliosis in alpha-**
945 **synucleinopathies: the emerging concept of primary gliodegeneration.** *Acta*
946 *Neuropathol* 2006, **112**:517-530.
- 947 7. Braak H, Sastre M, Del Tredici K: **Development of alpha-synuclein immunoreactive**
948 **astrocytes in the forebrain parallels stages of intraneuronal pathology in sporadic**
949 **Parkinson's disease.** *Acta Neuropathol* 2007, **114**:231-241.
- 950 8. Rostami J, Fotaki G, Sirois J, Mzezewa R, Bergstrom J, Essand M, Healy L, Erlandsson
951 A: **Astrocytes have the capacity to act as antigen-presenting cells in the Parkinson's**
952 **disease brain.** *J Neuroinflammation* 2020, **17**:119.
- 953 9. Rostami J, Holmqvist S, Lindstrom V, Sigvardson J, Westermark GT, Ingelsson M,
954 Bergstrom J, Roybon L, Erlandsson A: **Human Astrocytes Transfer Aggregated**
955 **Alpha-Synuclein via Tunneling Nanotubes.** *J Neurosci* 2017, **37**:11835-11853.
- 956 10. Biskup S, Moore DJ, Rea A, Lorenz-Deperieux B, Coombes CE, Dawson VL, Dawson
957 TM, West AB: **Dynamic and redundant regulation of LRRK2 and LRRK1**
958 **expression.** *BMC Neurosci* 2007, **8**:102.
- 959 11. Booth HDE, Hirst WD, Wade-Martins R: **The Role of Astrocyte Dysfunction in**
960 **Parkinson's Disease Pathogenesis.** *Trends Neurosci* 2017, **40**:358-370.
- 961 12. Henry AG, Aghamohammadzadeh S, Samaroo H, Chen Y, Mou K, Needle E, Hirst
962 WD: **Pathogenic LRRK2 mutations, through increased kinase activity, produce**
963 **enlarged lysosomes with reduced degradative capacity and increase ATP13A2**
964 **expression.** *Hum Mol Genet* 2015, **24**:6013-6028.

- 965 13. Tolosa E, Vila M, Klein C, Rascol O: **LRRK2 in Parkinson disease: challenges of**
966 **clinical trials.** *Nat Rev Neurol* 2020, **16**:97-107.
- 967 14. Alessi DR, Sammler E: **LRRK2 kinase in Parkinson's disease.** *Science* 2018, **360**:36-
968 37.
- 969 15. Martin I, Dawson VL, Dawson TM: **Recent advances in the genetics of Parkinson's**
970 **disease.** *Annu Rev Genomics Hum Genet* 2011, **12**:301-325.
- 971 16. Cogo S, Manzoni C, Lewis PA, Greggio E: **Leucine-rich repeat kinase 2 and**
972 **lysosomal dyshomeostasis in Parkinson disease.** *J Neurochem* 2020, **152**:273-283.
- 973 17. Cookson MR: **Mechanisms of Mutant LRRK2 Neurodegeneration.** *Adv Neurobiol*
974 2017, **14**:227-239.
- 975 18. Chen J, Chen Y, Pu J: **Leucine-Rich Repeat Kinase 2 in Parkinson's Disease:**
976 **Updated from Pathogenesis to Potential Therapeutic Target.** *Eur Neurol* 2018,
977 **79**:256-265.
- 978 19. Schapansky J, Khasnavis S, DeAndrade MP, Nardoizzi JD, Falkson SR, Boyd JD,
979 Sanderson JB, Bartels T, Melrose HL, LaVoie MJ: **Familial knockin mutation of**
980 **LRRK2 causes lysosomal dysfunction and accumulation of endogenous insoluble**
981 **alpha-synuclein in neurons.** *Neurobiol Dis* 2018, **111**:26-35.
- 982 20. Tong Y, Giaime E, Yamaguchi H, Ichimura T, Liu Y, Si H, Cai H, Bonventre JV, Shen
983 J: **Loss of leucine-rich repeat kinase 2 causes age-dependent bi-phasic alterations**
984 **of the autophagy pathway.** *Mol Neurodegener* 2012, **7**:2.
- 985 21. Bieri G, Brahic M, Bousset L, Couthouis J, Kramer NJ, Ma R, Nakayama L, Monbureau
986 M, Defensor E, Schule B, et al: **LRRK2 modifies alpha-syn pathology and spread in**
987 **mouse models and human neurons.** *Acta Neuropathol* 2019, **137**:961-980.
- 988 22. Kim KS, Marcogliese PC, Yang J, Callaghan SM, Resende V, Abdel-Messih E, Marras
989 C, Visanji NP, Huang J, Schlossmacher MG, et al: **Regulation of myeloid cell**

phagocytosis by LRRK2 via WAVE2 complex stabilization is altered in Parkinson's disease. *Proc Natl Acad Sci U S A* 2018, **115**:E5164-E5173.

23. Marker DF, Puccini JM, Mockus TE, Barbieri J, Lu SM, Gelbard HA: **LRRK2 kinase inhibition prevents pathological microglial phagocytosis in response to HIV-1 Tat protein.** *J Neuroinflammation* 2012, **9**:261.

24. Sanyal A, DeAndrade MP, Novis HS, Lin S, Chang J, Lengacher N, Tomlinson JJ, Tansey MG, LaVoie MJ: **Lysosome and Inflammatory Defects in GBA1-Mutant Astrocytes Are Normalized by LRRK2 Inhibition.** *Mov Disord* 2020, **35**:760-773.

25. Hartlova A, Herbst S, Peltier J, Rodgers A, Bilkei-Gorzo O, Fearn A, Dill BD, Lee H, Flynn R, Cowley SA, et al: **LRRK2 is a negative regulator of Mycobacterium tuberculosis phagosome maturation in macrophages.** *EMBO J* 2018, **37**.

26. Lee H, Flynn R, Sharma I, Haberman E, Carling PJ, Nicholls FJ, Stegmann M, Vowles J, Haenseler W, Wade-Martins R, et al: **LRRK2 Is Recruited to Phagosomes and Co-recruits RAB8 and RAB10 in Human Pluripotent Stem Cell-Derived Macrophages.** *Stem Cell Reports* 2020, **14**:940-955.

27. Liu Z, Xu E, Zhao HT, Cole T, West AB: **LRRK2 and Rab10 coordinate macropinocytosis to mediate immunological responses in phagocytes.** *EMBO J* 2020:e104862.

28. Sofroniew MV, Vinters HV: **Astrocytes: biology and pathology.** *Acta Neuropathol* 2010, **119**:7-35.

29. Loov C, Hillered L, Ebendal T, Erlandsson A: **Engulfing astrocytes protect neurons from contact-induced apoptosis following injury.** *PLoS One* 2012, **7**:e33090.

30. Loov C, Mitchell CH, Simonsson M, Erlandsson A: **Slow degradation in phagocytic astrocytes can be enhanced by lysosomal acidification.** *Glia* 2015, **63**:1997-2009.

- 1014 31. Sollvander S, Nikitidou E, Brolin R, Soderberg L, Sehlin D, Lannfelt L, Erlandsson A:
1015 **Accumulation of amyloid-beta by astrocytes result in enlarged endosomes and**
1016 **microvesicle-induced apoptosis of neurons.** *Mol Neurodegener* 2016, **11**:38.
- 1017 32. Lindstrom V, Gustafsson G, Sanders LH, Howlett EH, Sigvardson J, Kasrayan A,
1018 Ingelsson M, Bergstrom J, Erlandsson A: **Extensive uptake of alpha-synuclein**
1019 **oligomers in astrocytes results in sustained intracellular deposits and**
1020 **mitochondrial damage.** *Mol Cell Neurosci* 2017, **82**:143-156.
- 1021 33. Loria F, Vargas JY, Bousset L, Syan S, Salles A, Melki R, Zurzolo C: **alpha-Synuclein**
1022 **transfer between neurons and astrocytes indicates that astrocytes play a role in**
1023 **degradation rather than in spreading.** *Acta Neuropathol* 2017, **134**:789-808.
- 1024 34. Ferrazza R, Cogo S, Melrose H, Bubacco L, Greggio E, Guella G, Civiero L, Plotegher
1025 N: **LRRK2 deficiency impacts ceramide metabolism in brain.** *Biochem Biophys Res*
1026 *Commun* 2016, **478**:1141-1146.
- 1027 35. Civiero L, Cirnaru MD, Beilina A, Rodella U, Russo I, Belluzzi E, Lobbestael E,
1028 Reyniers L, Hondhamuni G, Lewis PA, et al: **Leucine-rich repeat kinase 2 interacts**
1029 **with p21-activated kinase 6 to control neurite complexity in mammalian brain.** *J*
1030 *Neurochem* 2015, **135**:1242-1256.
- 1031 36. Longo F, Mercatelli D, Novello S, Arcuri L, Brugnoli A, Vincenzi F, Russo I, Berti G,
1032 Mabrouk OS, Kennedy RT, et al: **Age-dependent dopamine transporter dysfunction**
1033 **and Serine129 phospho-alpha-synuclein overload in G2019S LRRK2 mice.** *Acta*
1034 *Neuropathol Commun* 2017, **5**:22.
- 1035 37. Davis AA, Temple S: **A self-renewing multipotential stem cell in embryonic rat**
1036 **cerebral cortex.** *Nature* 1994, **372**:263-266.

- 1037 38. Johe KK, Hazel TG, Muller T, Dugich-Djordjevic MM, McKay RD: **Single factors**
1038 **direct the differentiation of stem cells from the fetal and adult central nervous**
1039 **system.** *Genes Dev* 1996, **10**:3129-3140.
- 1040 39. Ravin R, Hoeppner DJ, Munno DM, Carmel L, Sullivan J, Levitt DL, Miller JL, Athaide
1041 C, Panchision DM, McKay RD: **Potency and fate specification in CNS stem cell**
1042 **populations in vitro.** *Cell Stem Cell* 2008, **3**:670-680.
- 1043 40. Sollvander S, Nikitidou E, Gallasch L, Zysk M, Soderberg L, Sehlin D, Lannfelt L,
1044 Erlandsson A: **The Abeta protofibril selective antibody mAb158 prevents**
1045 **accumulation of Abeta in astrocytes and rescues neurons from Abeta-induced cell**
1046 **death.** *J Neuroinflammation* 2018, **15**:98.
- 1047 41. Civiero L, Vancraenenbroeck R, Belluzzi E, Beilina A, Lobbestael E, Reyniers L, Gao
1048 F, Micetic I, De Maeyer M, Bubacco L, et al: **Biochemical characterization of highly**
1049 **purified leucine-rich repeat kinases 1 and 2 demonstrates formation of**
1050 **homodimers.** *PLoS One* 2012, **7**:e43472.
- 1051 42. Codolo G, Plotegher N, Pozzobon T, Brucale M, Tessari I, Bubacco L, de Bernard M:
1052 **Triggering of inflammasome by aggregated alpha-synuclein, an inflammatory**
1053 **response in synucleinopathies.** *PLoS One* 2013, **8**:e55375.
- 1054 43. Pivato M, De Franceschi G, Tosatto L, Frare E, Kumar D, Aioanei D, Brucale M,
1055 Tessari I, Bisaglia M, Samori B, et al: **Covalent alpha-synuclein dimers: chemico-**
1056 **physical and aggregation properties.** *PLoS One* 2012, **7**:e50027.
- 1057 44. Kim Y, Ho SO, Gassman NR, Korlann Y, Landorf EV, Collart FR, Weiss S: **Efficient**
1058 **site-specific labeling of proteins via cysteines.** *Bioconjug Chem* 2008, **19**:786-791.
- 1059 45. Hurbain I, Romao M, Bergam P, Heiligenstein X, Raposo G: **Analyzing Lysosome-**
1060 **Related Organelles by Electron Microscopy.** *Methods Mol Biol* 2017, **1594**:43-71.

- 1061 46. Carraro M, Checchetto V, Sartori G, Kucharczyk R, di Rago JP, Minervini G, Franchin
1062 C, Arrigoni G, Giorgio V, Petronilli V, et al: **High-Conductance Channel Formation**
1063 **in Yeast Mitochondria is Mediated by F-ATP Synthase e and g Subunits.** *Cell*
1064 *Physiol Biochem* 2018, **50**:1840-1855.
- 1065 47. Gustafsson G, Lindstrom V, Rostami J, Nordstrom E, Lannfelt L, Bergstrom J,
1066 Ingelsson M, Erlandsson A: **Alpha-synuclein oligomer-selective antibodies reduce**
1067 **intracellular accumulation and mitochondrial impairment in alpha-synuclein**
1068 **exposed astrocytes.** *J Neuroinflammation* 2017, **14**:241.
- 1069 48. Middeldorp J, Hol EM: **GFAP in health and disease.** *Prog Neurobiol* 2011, **93**:421-
1070 443.
- 1071 49. Westerlund M, Belin AC, Anvret A, Bickford P, Olson L, Galter D: **Developmental**
1072 **regulation of leucine-rich repeat kinase 1 and 2 expression in the brain and other**
1073 **rodent and human organs: Implications for Parkinson's disease.** *Neuroscience*
1074 2008, **152**:429-436.
- 1075 50. Giesert F, Hofmann A, Burger A, Zerle J, Kloos K, Hafen U, Ernst L, Zhang J, Vogt-
1076 Weisenhorn DM, Wurst W: **Expression analysis of Lrrk1, Lrrk2 and Lrrk2 splice**
1077 **variants in mice.** *PLoS One* 2013, **8**:e63778.
- 1078 51. Hawrysh PJ, Buck LT: **Mitochondrial matrix pH acidifies during anoxia and is**
1079 **maintained by the F1Fo-ATPase in anoxia-tolerant painted turtle cortical neurons.**
1080 *FEBS Open Bio* 2019, **9**:571-581.
- 1081 52. Lerch S, Ritz S, Bley K, Messerschmidt C, Weiss CK, Musyanovych A, Landfester K,
1082 Mailander V: **Nanoprobng the acidification process during intracellular uptake**
1083 **and trafficking.** *Nanomedicine* 2015, **11**:1585-1596.
- 1084 53. Repetto G, del Peso A, Zurita JL: **Neutral red uptake assay for the estimation of cell**
1085 **viability/cytotoxicity.** *Nat Protoc* 2008, **3**:1125-1131.

- 1086 54. Pinsino A, Russo R, Bonaventura R, Brunelli A, Marcomini A, Matranga V: **Titanium**
1087 **dioxide nanoparticles stimulate sea urchin immune cell phagocytic activity**
1088 **involving TLR/p38 MAPK-mediated signalling pathway.** *Sci Rep* 2015, **5**:14492.
- 1089 55. Shen K, Sidik H, Talbot WS: **The Rag-Ragulator Complex Regulates Lysosome**
1090 **Function and Phagocytic Flux in Microglia.** *Cell Rep* 2016, **14**:547-559.
- 1091 56. Law AL, Ling Q, Hajjar KA, Futter CE, Greenwood J, Adamson P, Wavre-Shapton ST,
1092 Moss SE, Hayes MJ: **Annexin A2 regulates phagocytosis of photoreceptor outer**
1093 **segments in the mouse retina.** *Mol Biol Cell* 2009, **20**:3896-3904.
- 1094 57. Scharf B, Clement CC, Wu XX, Morozova K, Zanolini D, Follenzi A, Larocca JN,
1095 Levon K, Sutterwala FS, Rand J, et al: **Annexin A2 binds to endosomes following**
1096 **organelle destabilization by particulate wear debris.** *Nat Commun* 2012, **3**:755.
- 1097 58. Li R, Tan S, Yu M, Jundt MC, Zhang S, Wu M: **Annexin A2 Regulates Autophagy in**
1098 **Pseudomonas aeruginosa Infection through the Akt1-mTOR-ULK1/2 Signaling**
1099 **Pathway.** *J Immunol* 2015, **195**:3901-3911.
- 1100 59. Moreau K, Ghislat G, Hochfeld W, Renna M, Zavodszky E, Runwal G, Puri C, Lee S,
1101 Siddiqi F, Menzies FM, et al: **Transcriptional regulation of Annexin A2 promotes**
1102 **starvation-induced autophagy.** *Nat Commun* 2015, **6**:8045.
- 1103 60. Morozova K, Sridhar S, Zolla V, Clement CC, Scharf B, Verzani Z, Diaz A, Larocca
1104 JN, Hajjar KA, Cuervo AM, Santambrogio L: **Annexin A2 promotes phagophore**
1105 **assembly by enhancing Atg16L(+) vesicle biogenesis and homotypic fusion.** *Nat*
1106 *Commun* 2015, **6**:5856.
- 1107 61. Bustos V, Pulina MV, Bispo A, Lam A, Flajolet M, Gorelick FS, Greengard P:
1108 **Phosphorylated Presenilin 1 decreases beta-amyloid by facilitating**
1109 **autophagosome-lysosome fusion.** *Proc Natl Acad Sci U S A* 2017, **114**:7148-7153.

- 1110 62. Choi I, Zhang Y, Seegobin SP, Pruvost M, Wang Q, Purtell K, Zhang B, Yue Z:
1111 **Microglia clear neuron-released alpha-synuclein via selective autophagy and**
1112 **prevent neurodegeneration.** *Nat Commun* 2020, **11**:1386.
- 1113 63. de Graauw M, Cao L, Winkel L, van Miltenburg MH, le Devedec SE, Klop M, Yan K,
1114 Pont C, Rogkoti VM, Tijssma A, et al: **Annexin A2 depletion delays EGFR endocytic**
1115 **trafficking via cofilin activation and enhances EGFR signaling and metastasis**
1116 **formation.** *Oncogene* 2014, **33**:2610-2619.
- 1117 64. Stukes S, Coelho C, Rivera J, Jedlicka AE, Hajjar KA, Casadevall A: **The Membrane**
1118 **Phospholipid Binding Protein Annexin A2 Promotes Phagocytosis and Nonlytic**
1119 **Exocytosis of Cryptococcus neoformans and Impacts Survival in Fungal Infection.**
1120 *J Immunol* 2016, **197**:1252-1261.
- 1121 65. Recasens A, Dehay B: **Alpha-synuclein spreading in Parkinson's disease.** *Frontiers*
1122 *in Neuroanatomy* 2014, **8**.
- 1123 66. Luk KC, Kehm VM, Zhang B, O'Brien P, Trojanowski JQ, Lee VMY: **Intracerebral**
1124 **inoculation of pathological α -synuclein initiates a rapidly progressive**
1125 **neurodegenerative α -synucleinopathy in mice.** *Journal of Experimental Medicine*
1126 2012, **209**:975-986.
- 1127 67. Kordower JH, Chu Y, Hauser RA, Freeman TB, Olanow CW: **Lewy body-like**
1128 **pathology in long-term embryonic nigral transplants in Parkinson's disease.**
1129 *Nature Medicine* 2008, **14**:504-506.
- 1130 68. Li J-Y, Englund E, Holton JL, Soulet D, Hagell P, Lees AJ, Lashley T, Quinn NP,
1131 Rehnkrone S, Björklund A, et al: **Lewy bodies in grafted neurons in subjects with**
1132 **Parkinson's disease suggest host-to-graft disease propagation.** *Nature Medicine*
1133 2008, **14**:501-503.

- 1134 69. Desplats P, Lee HJ, Bae EJ, Patrick C, Rockenstein E, Crews L, Spencer B, Masliah E,
1135 Lee SJ: **Inclusion formation and neuronal cell death through neuron-to-neuron**
1136 **transmission of α -synuclein.** *Proceedings of the National Academy of Sciences* 2009,
1137 **106:**13010-13015.
- 1138 70. Hansen C, Angot E, Bergström A-L, Steiner JA, Pieri L, Paul G, Outeiro TF, Melki R,
1139 Kallunki P, Fog K, et al: **α -Synuclein propagates from mouse brain to grafted**
1140 **dopaminergic neurons and seeds aggregation in cultured human cells.** *Journal of*
1141 *Clinical Investigation* 2011, **121:**715-725.
- 1142 71. Angot E, Steiner JA, Lema Tome CM, Ekstrom P, Mattsson B, Bjorklund A, Brundin
1143 P: **Alpha-synuclein cell-to-cell transfer and seeding in grafted dopaminergic**
1144 **neurons in vivo.** *PLoS One* 2012, **7:**e39465.
- 1145 72. Lee HJ, Patel S, Lee SJ: **Intravesicular localization and exocytosis of alpha-**
1146 **synuclein and its aggregates.** *J Neurosci* 2005, **25:**6016-6024.
- 1147 73. Emmanouilidou E, Elenis D, Papasilekas T, Stranjalis G, Gerozissis K, Ioannou PC,
1148 Vekrellis K: **Assessment of alpha-synuclein secretion in mouse and human brain**
1149 **parenchyma.** *PLoS One* 2011, **6:**e22225.
- 1150 74. Reyes JF, Olsson TT, Lamberts JT, Devine MJ, Kunath T, Brundin P: **A cell culture**
1151 **model for monitoring α -synuclein cell-to-cell transfer.** *Neurobiology of Disease*
1152 2015, **77:**266-275.
- 1153 75. Lee H-J, Suk J-E, Patrick C, Bae E-J, Cho J-H, Rho S, Hwang D, Masliah E, Lee S-J:
1154 **Direct Transfer of α -Synuclein from Neuron to Astroglia Causes Inflammatory**
1155 **Responses in Synucleinopathies.** *Journal of Biological Chemistry* 2010, **285:**9262-
1156 9272.

- 1157 76. Danzer KM, Ruf WP, Putcha P, Joyner D, Hashimoto T, Glabe C, Hyman BT, McLean
1158 PJ: **Heat-shock protein 70 modulates toxic extracellular alpha-synuclein oligomers**
1159 **and rescues trans-synaptic toxicity.** *FASEB J* 2011, **25**:326-336.
- 1160 77. Zhao Y, Keshiya S, Atashrazm F, Gao J, Ittner LM, Alessi DR, Halliday GM, Fu Y,
1161 Dzamko N: **Nigrostriatal pathology with reduced astrocytes in LRRK2 S910/S935**
1162 **phosphorylation deficient knockin mice.** *Neurobiol Dis* 2018, **120**:76-87.
- 1163 78. Lee JH, Han JH, Kim H, Park SM, Joe EH, Jou I: **Parkinson's disease-associated**
1164 **LRRK2-G2019S mutant acts through regulation of SERCA activity to control ER**
1165 **stress in astrocytes.** *Acta Neuropathol Commun* 2019, **7**:68.
- 1166 79. di Domenico A, Carola G, Calatayud C, Pons-Espinal M, Munoz JP, Richaud-Patin Y,
1167 Fernandez-Carasa I, Gut M, Faella A, Parameswaran J, et al: **Patient-Specific iPSC-**
1168 **Derived Astrocytes Contribute to Non-Cell-Autonomous Neurodegeneration in**
1169 **Parkinson's Disease.** *Stem Cell Reports* 2019, **12**:213-229.
- 1170 80. Lara Ordonez AJ, Fernandez B, Fdez E, Romo-Lozano M, Madero-Perez J, Lobbestael
1171 E, Baekelandt V, Aiastui A, Lopez de Munain A, Melrose HL, et al: **RAB8, RAB10**
1172 **and RILPL1 contribute to both LRRK2 kinase-mediated centrosomal cohesion**
1173 **and ciliogenesis deficits.** *Hum Mol Genet* 2019, **28**:3552-3568.
- 1174 81. Booth HDE, Wessely F, Connor-Robson N, Rinaldi F, Vowles J, Browne C, Evetts SG,
1175 Hu MT, Cowley SA, Webber C, Wade-Martins R: **RNA sequencing reveals MMP2**
1176 **and TGFB1 downregulation in LRRK2 G2019S Parkinson's iPSC-derived**
1177 **astrocytes.** *Neurobiol Dis* 2019, **129**:56-66.
- 1178 82. Hyttinen JMT, Amadio M, Viiri J, Pascale A, Salminen A, Kaarniranta K: **Clearance**
1179 **of misfolded and aggregated proteins by aggrephagy and implications for**
1180 **aggregation diseases.** *Ageing Research Reviews* 2014, **18**:16-28.

- 1181 83. Baptista MA, Dave KD, Frasier MA, Sherer TB, Greeley M, Beck MJ, Varsho JS,
 1182 Parker GA, Moore C, Churchill MJ, et al: **Loss of leucine-rich repeat kinase 2**
 1183 **(LRRK2) in rats leads to progressive abnormal phenotypes in peripheral organs.**
 1184 *PLoS One* 2013, **8**:e80705.
- 1185 84. Walter J, Bolognin S, Antony PMA, Nickels SL, Poovathingal SK, Salamanca L, Magni
 1186 S, Perfeito R, Hoel F, Qing X, et al: **Neural Stem Cells of Parkinson's Disease**
 1187 **Patients Exhibit Aberrant Mitochondrial Morphology and Functionality.** *Stem Cell*
 1188 *Reports* 2019, **12**:878-889.
- 1189 85. Hipolito VEB, Diaz JA, Tandoc KV, Oertlin C, Ristau J, Chauhan N, Saric A,
 1190 McLaughlan S, Larsson O, Topisirovic I, Botelho RJ: **Enhanced translation expands**
 1191 **the endo-lysosome size and promotes antigen presentation during phagocyte**
 1192 **activation.** *PLoS Biol* 2019, **17**:e3000535.
- 1193 86. Mayran N, Parton RG, Gruenberg J: **Annexin II regulates multivesicular endosome**
 1194 **biogenesis in the degradation pathway of animal cells.** *EMBO J* 2003, **22**:3242-3253.
- 1195 87. Grieve AG, Moss SE, Hayes MJ: **Annexin A2 at the interface of actin and membrane**
 1196 **dynamics: a focus on its roles in endocytosis and cell polarization.** *Int J Cell Biol*
 1197 2012, **2012**:852430.
- 1198 88. Eberhard DA, Brown MD, VandenBerg SR: **Alterations of annexin expression in**
 1199 **pathological neuronal and glial reactions. Immunohistochemical localization of**
 1200 **annexins I, II (p36 and p11 subunits), IV, and VI in the human hippocampus.** *Am*
 1201 *J Pathol* 1994, **145**:640-649.
- 1202 89. Juul-Madsen K, Qvist P, Bendtsen KL, Langkilde AE, Vestergaard B, Howard KA,
 1203 Dehesa-Etxebeste M, Paludan SR, Andersen GR, Jensen PH, et al: **Size-Selective**
 1204 **Phagocytic Clearance of Fibrillar alpha-Synuclein through Conformational**
 1205 **Activation of Complement Receptor 4.** *J Immunol* 2020, **204**:1345-1361.

1206 90. Zhang Q, Xu Y, Lee J, Jarnik M, Wu X, Bonifacino JS, Shen J, Ye Y: **A myosin-7B-**
1207 **dependent endocytosis pathway mediates cellular entry of alpha-synuclein fibrils**
1208 **and polycation-bearing cargos.** *Proc Natl Acad Sci U S A* 2020, **117**:10865-10875.

1209 91. Rodriguez L, Marano MM, Tandon A: **Import and Export of Misfolded alpha-**
1210 **Synuclein.** *Front Neurosci* 2018, **12**:344.

1211

1212

1213

1214

1215

1216

1217

1218

1219

1220

1221

1222

1223

1224

1225

1226

Figures

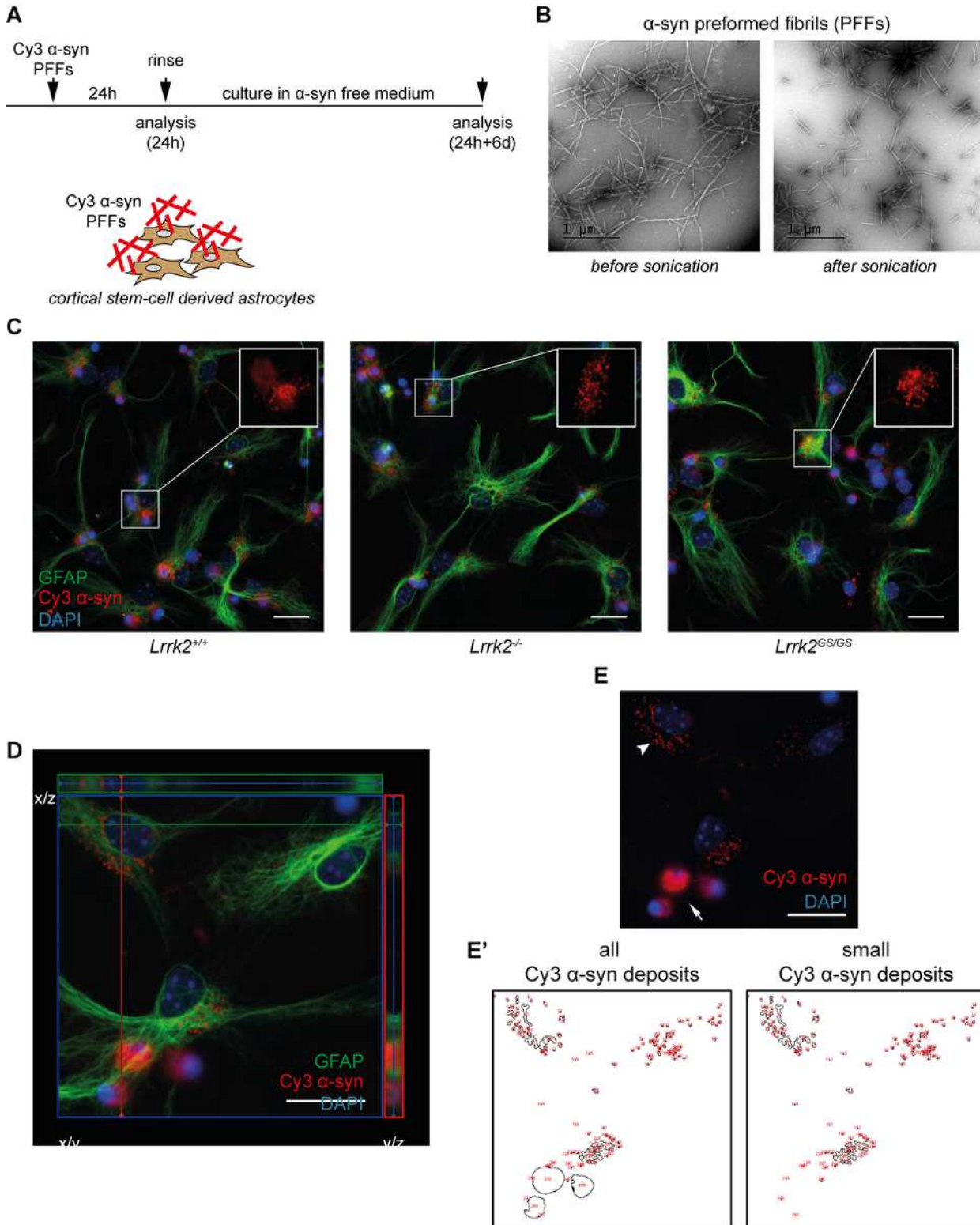
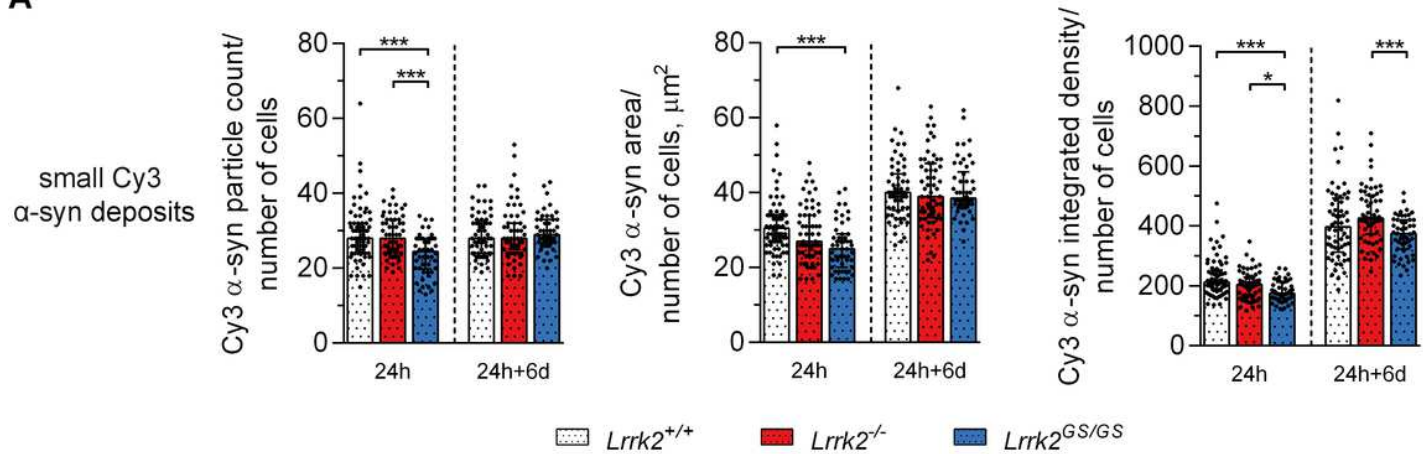


Figure 1

Accumulation of aggregated α -syn in *Lrrk2* astrocytes. A) Schematic outline of the experimental set-up. Cells were exposed to 0.5 μ M sonicated Cy3 α -syn PFFs for 24 h. B) TEM images of α -syn PFFs pre and post sonication. Scale bars 1 μ m. C) Representative fluorescence microscopy images of *Lrrk2*^{+/+}, *Lrrk2*^{-/-}, *Lrrk2*^{GS/GS}

and Lrrk2GS/GS astrocytes (GFAP, green) at 24 h; cell nuclei stained with DAPI (blue) and α -syn labeled with Cy3 (red). Insets show a close-up of Cy3 α -syn inclusions. D) Orthogonal projections of z-stack images taken with a fluorescence microscope: main view (x/y), top (x/z) and right (y/z). Projections were made along the lines depicted in the main image. Astrocytes (GFAP, green), Cy3 labeled α -syn (red), DAPI (blue). E) Fluorescence microscopy image showing the differently sized Cy3 α -syn inclusions observed: small dot-like inclusions (arrow head) and larger, cottony deposits (arrow). E') Displays of the particle count obtained from the ImageJ analysis when including either all Cy3 α -syn deposits or only the small Cy3 α -syn inclusions. Scale bars = 20 μ m (C, D and E).

A



B

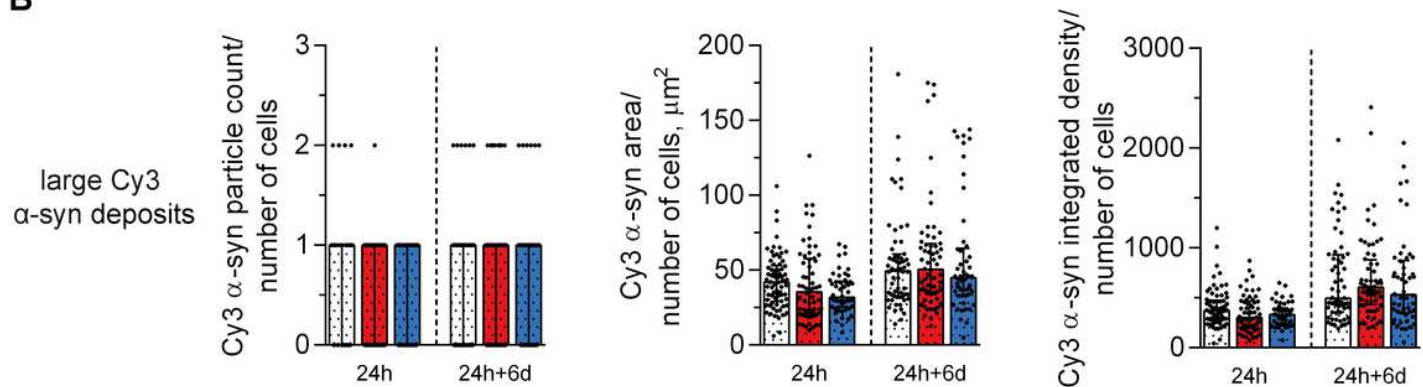


Figure 2

Analysis of the differently sized α -syn inclusions in Lrrk2 astrocytes. A and B) Analysis of small and large Cy3 α -syn inclusions, respectively. Quantifications of Cy3 α -syn particle count, total area and integrated density were performed using ImageJ. For both time-points ten images per independent cell culture (24 h: Lrrk1+/+ n = 7, Lrrk2^{-/-} n = 6 and Lrrk2GS/GS n = 5; 24 h + 6 d: Lrrk1+/+ n = 6, Lrrk2^{-/-} n = 6 and Lrrk2GS/GS n = 5) were analyzed and reported. For each time-point, the statistical analysis was performed with the Kruskal- Wallis test followed by Dunn's multiple comparisons test, since the data did not follow Gaussian distribution for all groups. * p \leq 0.05 ** p \leq 0.01 *** p \leq 0.001

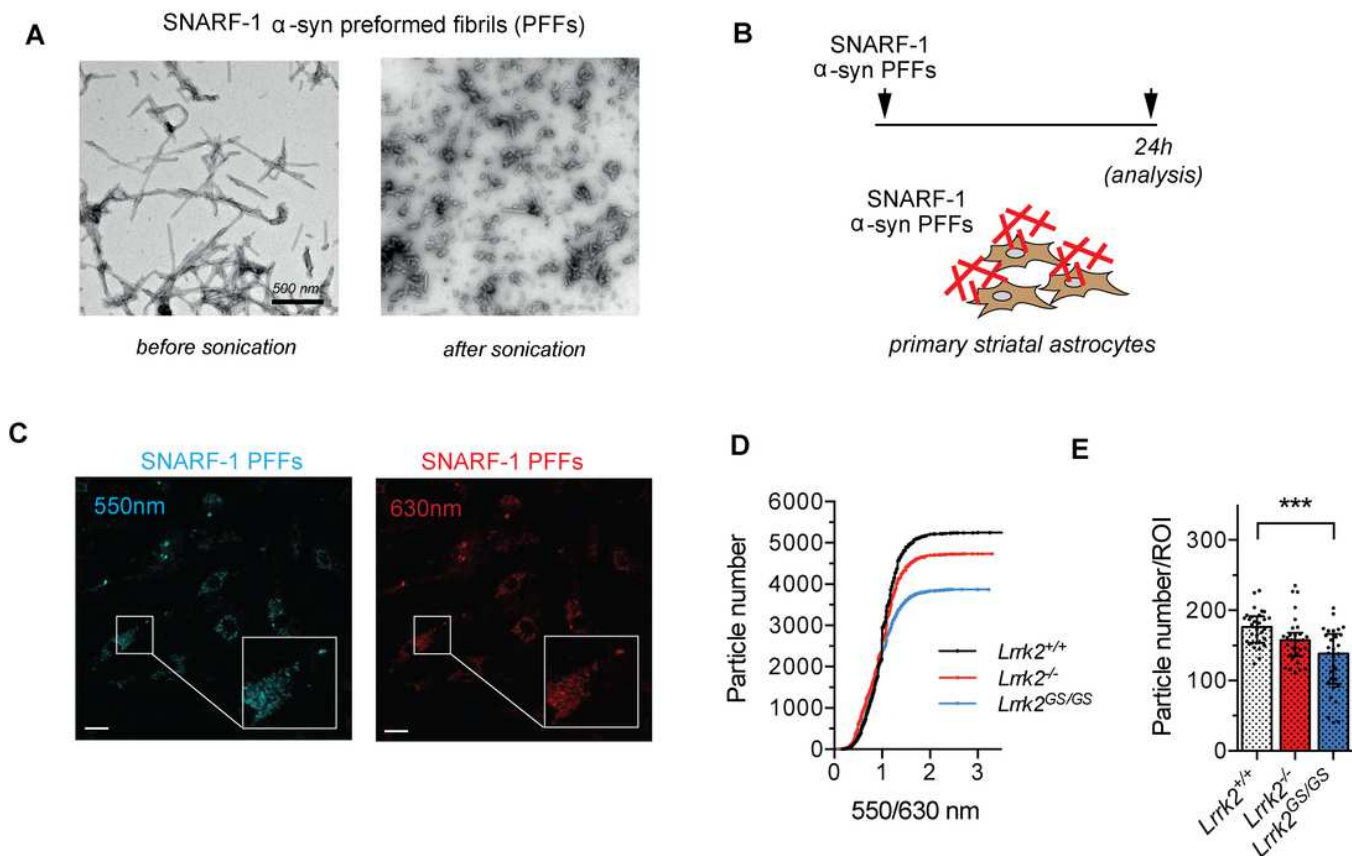


Figure 3

Internalization of aggregated α -syn in striatal astrocytes. A) TEM images of SNARF-1 α -syn PFFs pre and post sonication. B) Schematic outline of the experimental set-up. Cells were exposed to 0.5 μ M sonicated SNARF-1 α -syn PFFs for 24 h and imaged using live confocal laser scanning microscopy. C) Representative images of primary $Lrrk2^{+/+}$ striatal astrocytes treated with SNARF-1 α -syn PFFs were acquired at range of 530-550 and 610-630 nm. Scale bar 50 μ m. D and E) Eight images per cell culture were analyzed ($n=4$ independent cultures). For each image, ROIs were traced and quantification of α -syn single-particle 550/630 ratio (IntDen) and number were performed using ImageJ. The cumulative distribution of the single-particle ratio was graphed for each genotype in D and particle number per ROI in E. Statistical analysis in E was performed using Kruskal-Wallis test followed by Dunn's multiple comparisons test. * $p \leq 0.05$ ** $p \leq 0.01$ *** $p \leq 0.001$

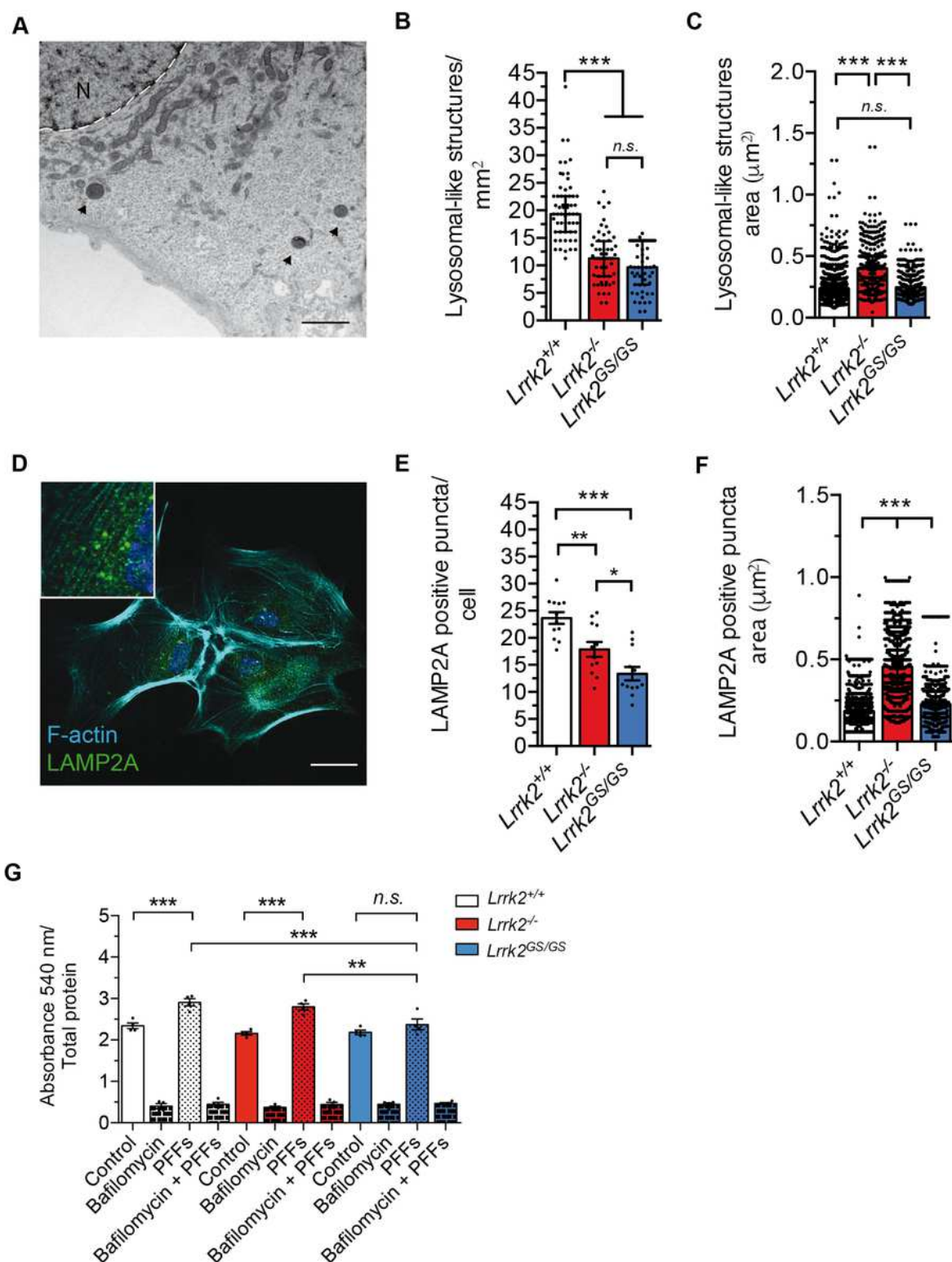


Figure 4

Description of the endo-lysosomal pathway in *Lrrk2* striatal astrocytes. A) Representative TEM image of primary striatal astrocyte section containing electron dense lysosomal-like structures (arrows). Scale bar 2 µm. B and C) Forty TEM images were acquired from n=4 per genotype. Each cell was imaged by covering the entire cytoplasm and lysosomal-like structure number and area were measured using ImageJ. D) Representative image of the staining using Lamp2A (green) as a marker for the endo-lysosomal pathway. E and F) Forty TEM images were acquired from n=4 per genotype. Each cell was imaged by covering the entire cytoplasm and LAMP2A positive puncta number and area were measured using ImageJ. G) Bar graph showing the absorbance at 540 nm per total protein for various treatments and genotypes. *** p < 0.001, ** p < 0.01, n.s. = not significant.

lysosomal pathway, DAPI (blue) for the nuclei and F-actin (cyano) to define cells. Scale bar 20 μ m. Inset shows a close-up of Lamp2A-positive structures. E and F) Four images per cell culture were analyzed (n=3 per genotype). G) Neutral red assay was performed in primary striatal astrocytes from the three genotypes upon unlabeled α -syn PPF treatment (n=4 per genotype). Bafilomycin has been applied as negative control. Absorbance at 540 nm measured upon cell lysates was normalized by total protein content. Quantifications of Lamp2A-positive structure number and area were analyzed using ImageJ. Statistical analysis in B, C and F was made by Kruskal-Wallis test followed by Dunn's multiple comparisons test. Statistical analysis in E and G was performed with one-way ANOVA followed by Tukey's multiple comparisons test. * $p \leq 0.05$ ** $p \leq 0.01$ *** $p \leq 0.001$

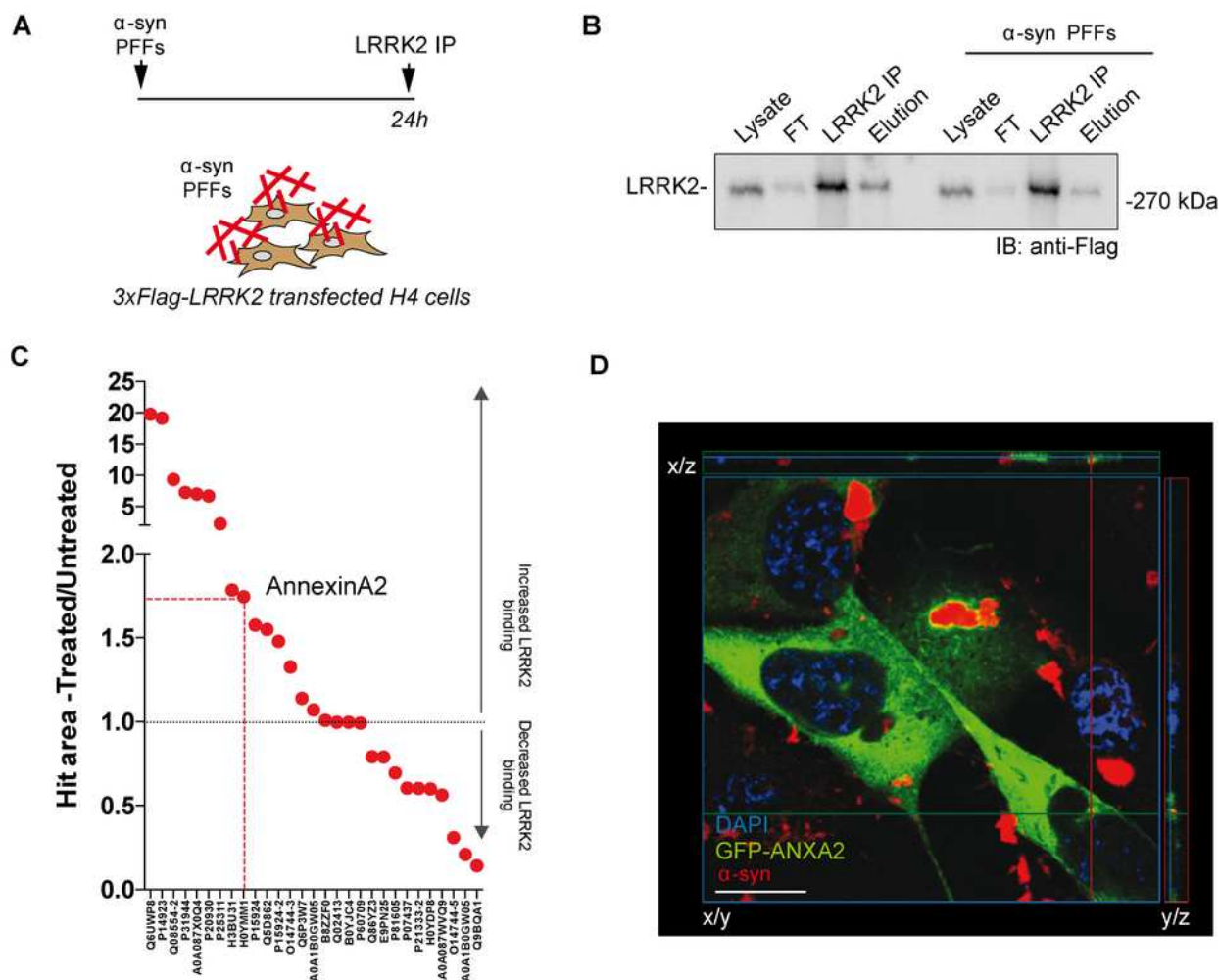


Figure 5

Characterization of LRRK2 interactoma in stimulated condition. A) Schematic outline of the experimental set-up. H4 cells were transfected using 3xFlag-LRRK2 encoding plasmid and, after 48 h post transfection, treated with 0.5 μ M sonicated unlabeled α -syn PFFs for 24 h. LRRK2 was subsequently immunopurified using anti-Flag agarose beads (IP), eluted with Flag peptide (elution) and subjected to LC-MS/MS analysis. FT: flow-through, unbound LRRK2. B) Western blot analysis showing LRRK2 expression,

immuno-purification and elution in H4 cells in treated and basal conditions. C) Relative quantification of LRRK2 interactome under treated and untreated conditions. The area of the precursor ions identified by LC-MS/MS analysis was used as a quantitative measure of the protein content. The ratio between the area of the precursor ions of untreated and treated samples (normalized by the content of LRRK2) was then considered to highlight proteins showing a different affinity for LRRK2 in the two conditions (n=2). D) H4 cells transfected with GFP-ANXA2 in α -syn PFF-treated condition verifying the proximity of internalized α -syn fibrils and transfected AnxA2. AnxA2-GFP (green), α -syn (red), DAPI (blue). Scale bar 30 μ m.

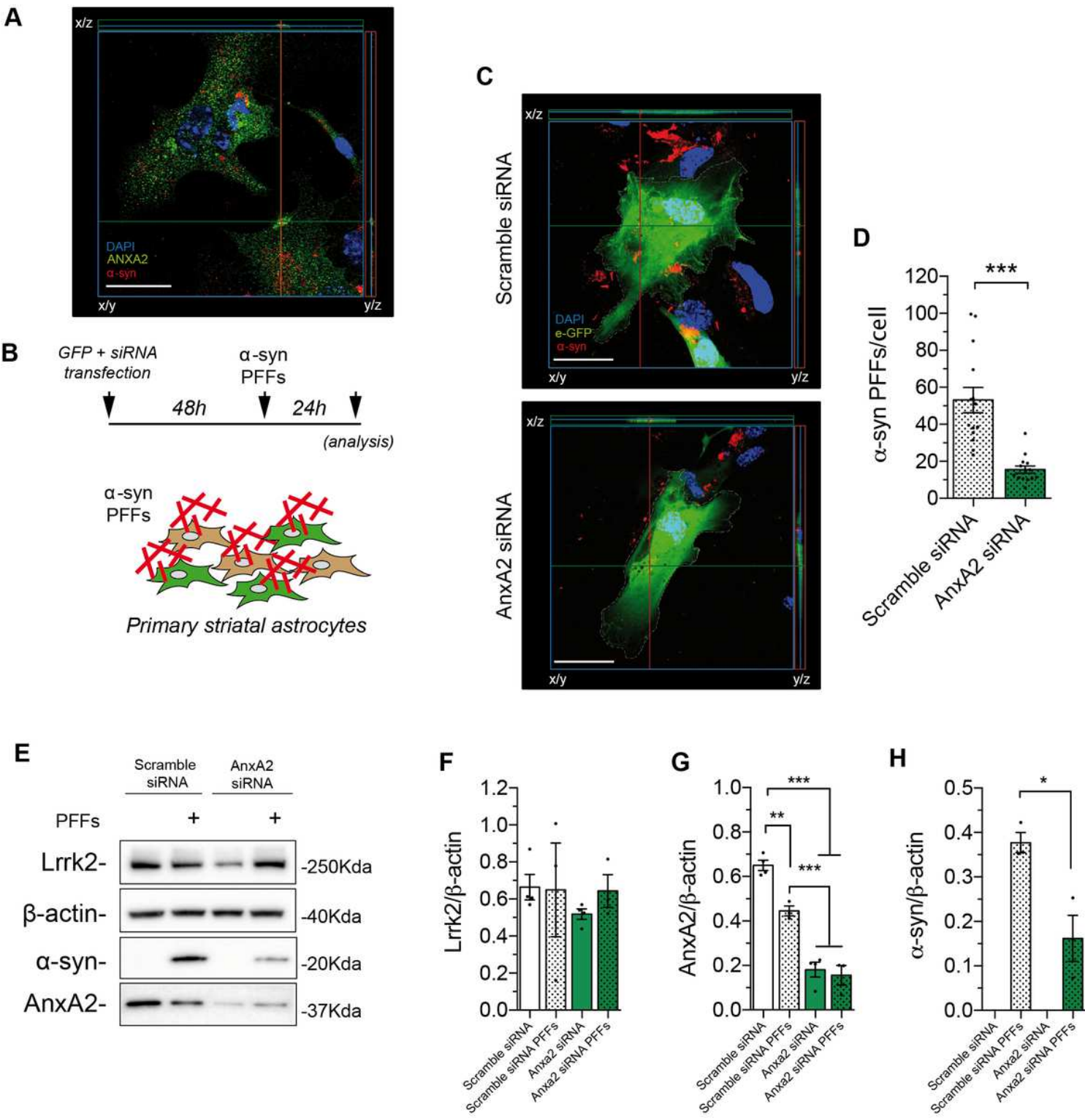


Figure 6

Investigation of AnxA2 function in astrocyte-mediated α -syn phagocytic clearance. A) Unlabeled α -syn PFFs have been applied to primary astrocytes for 24 h. Projections verify the proximity of the internalized α -syn fibrils and endogenous AnxA2. Cell cytoskeleton (F-actin, cyano), α -syn (red), AnxA2 (green), DAPI (blue). Scale bar 20 μ m. B) Schematic outline of the experimental set-up. Cells were transfected using 3xFlag-GFP encoding plasmid together with scramble or AnxA2 siRNA. 48 h post transfection cells were treated with 0.5 μ M sonicated α syn PFFs for 24 h and imaged using confocal microscopy. C) Representative images of primary striatal astrocytes transfected with scramble or Anxa2 siRNA together with a GFP-encoding plasmid in α -syn PFF839 treated condition. Projections verify the proximity of the internalized α -syn fibrils; GFP (green), α -syn (red), DAPI (blue). Scale bar 30 μ m. D) Four images per cell culture were analyzed (n=3). Quantifications of α -syn PFFs fluorescent positive puncta were performed using ImageJ (ComDet plugin). E) Western blot analysis of primary striatal astrocyte lysates transfected with scramble and AnxA2 siRNA under basal and PFF-treated conditions. Anti-Lrrk2, anti- α -syn and anti-AnxA2 antibodies have been employed. F, G and H) Quantification of band intensity was performed using ImageJ and normalized by β - actin (n=3). Statistical analysis in D was made by Kruskal-Wallis test followed by Dunn's multiple comparisons test. Statistical analysis in F, G and H was performed with an unpaired t-test or one-way ANOVA followed by Tukey's multiple comparisons test. * $p \leq 0.05$ ** $p \leq 0.01$ *** $p \leq 0.001$

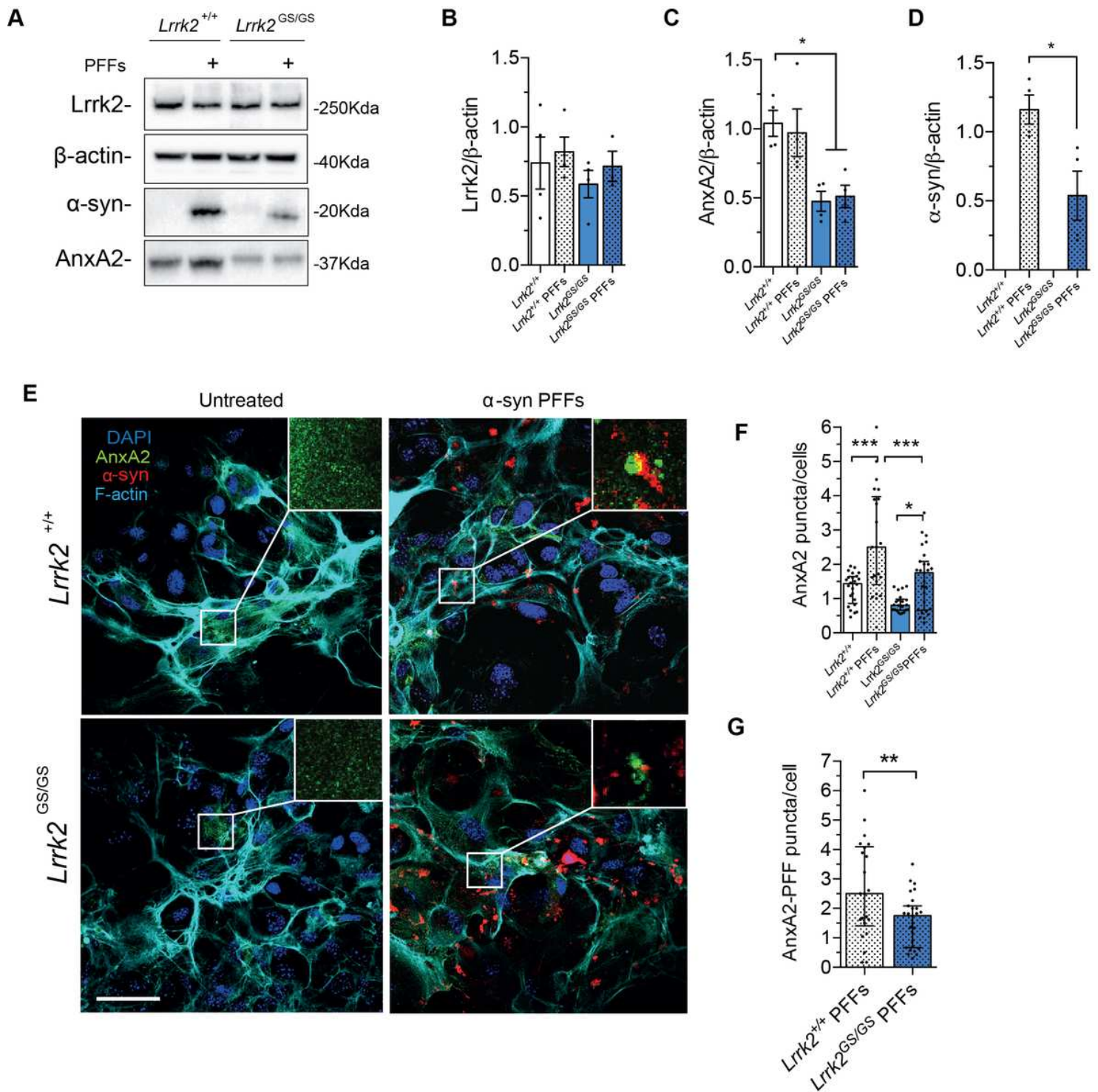


Figure 7

Analysis of AnxA2 function in G2019S primary striatal astrocytes at endogenous level. A) Western blot analysis of primary striatal astrocyte lysates under PFF-treated and basal conditions using anti-Lrrk2, anti-α-syn and anti-AnxA2 antibodies. B, C and D) Quantification of band intensity was performed using ImageJ and normalized by β-actin (n=4). E) Representative images of *Lrrk2*^{+/+} and *Lrrk2*^{GS/GS} astrocytes treated or not with α-syn PFFs and stained with anti-AnxA2 (green), anti-α-syn (red), F-actin (cyan) and cell nuclei with DAPI (blue). Scale bar 20 μm. Insets show a close-up of α-syn inclusions and

re-localized AnxA2. F and G) Eight images per cell culture were analyzed (n=3). Quantifications of Anxa2 puncta and AnxA2- α -syn PFFs proximity were performed using ImageJ. Statistical analysis in F and G was made by Kruskal-Wallis test followed by Dunn's multiple comparisons test. Statistical analysis in B, C and D was performed with unpaired t-test or one-way ANOVA followed by Tukey's multiple comparisons test. * $p \leq 0.05$ ** $p \leq 0.01$ *** $p \leq 0.001$

Supplementary Files

This is a list of supplementary files associated with this preprint. Click to download.

- [AdditionalFile1Final.pdf](#)